Device

Article

A wireless forehead e-tattoo for mental workload estimation

Graphical abstract

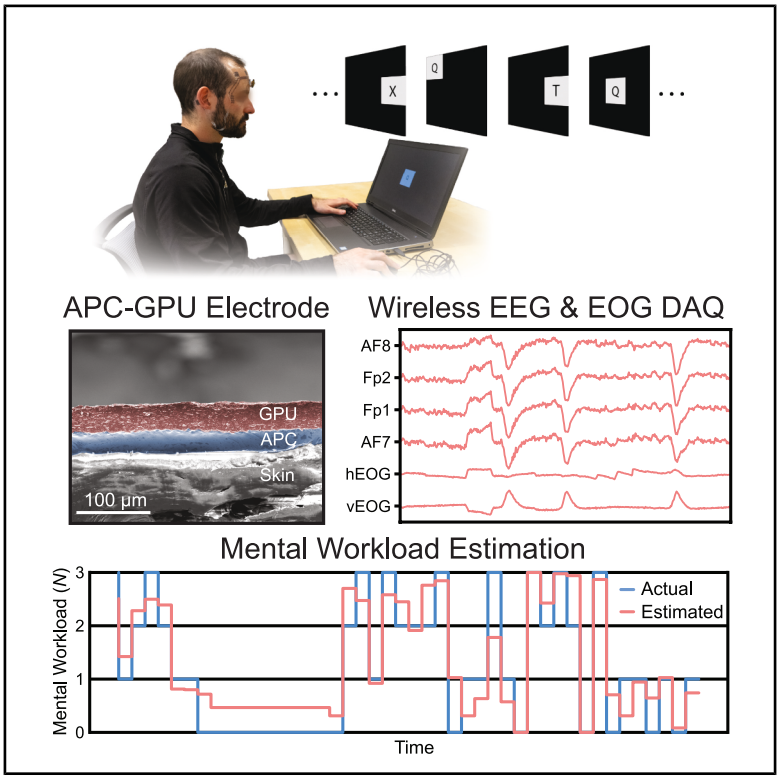

Highlights

- A wireless e-tattoo enables stable EEG and EOG monitoring during tasks
- APC-GPU electrodes enhance adhesion and reduce motion artifacts
- Mental workload is decoded using forehead EEG and EOG features and machine learning
- The ultra-thin design ensures comfort and compatibility with headgear

Authors

Heeyong Huh, Hyonyoung Shin, Hongbian Li, ..., Kathryn A. Feltman, Luis Sentis, Nanshu Lu

Correspondence

lsentis@utexas.edu (L.S.), nanshulu@utexas.edu (N.L.)

In brief

Huh et al. developed a wireless forehead e-tattoo for EEG- and EOG-based mental workload estimation. The e-tattoo features motion-resistant APC-GPU electrodes that enable stable, high-fidelity signal acquisition. Using a dual *N*-back cognitive task, the study demonstrates a strong correlation between physiological signals and workload levels. A machine-learning model trained on these signals successfully estimates workload variations, highlighting the system's feasibility as a compact, reliable alternative to conventional bulky EEG and EOG devices.

Validate
Functional device with real-world testing, ready to scale

Huh et al., 2025, Device *3*, 100781
August 15, 2025
https://doi.org/10.1016/j.device.2025.100781

CellPress

Please cite this article in press as: Huh et al., A wireless forehead e-tattoo for mental workload estimation, Device (2025), https://doi.org/10.1016/j.device.2025.100781

Device

CellPress

Article

A wireless forehead e-tattoo for mental workload estimation

Heeyong Huh,[1,7] Hyonyoung Shin,[2,7] Hongbian Li,[1] Kazuma Hirota,[3] Carolyn Hoang,[2] Shrikar Thangavel,[2] Matthew D'Alessandro,[4] Kathryn A. Feltman,[4] Luis Sentis,[1,*] and Nanshu Lu[1,2,3,5,6,8,*]

[1]Department of Aerospace Engineering and Engineering Mechanics, The University of Texas at Austin, Austin, TX 78712, USA
[2]Department of Electrical and Computer Engineering, The University of Texas at Austin, Austin, TX 78712, USA
[3]Department of Mechanical Engineering, The University of Texas at Austin, Austin, TX 78712, USA
[4]U.S. Army Aeromedical Research Laboratory, Fort Novosel, AL 36362, USA
[5]Department of Biomedical Engineering, The University of Texas at Austin, Austin, TX 78712, USA
[6]Texas Materials Institute, The University of Texas at Austin, Austin, TX 78712, USA
[7]These authors contributed equally
[8]Lead contact
*Correspondence: lsentis@utexas.edu (L.S.), nanshulu@utexas.edu (N.L.)
https://doi.org/10.1016/j.device.2025.100781

THE BIGGER PICTURE Mental workload is a critical factor in human-in-the-loop systems, directly influencing cognitive performance and decision making in high-stakes environments such as aviation, healthcare, and robotics. While electroencephalography (EEG) and electrooculography (EOG) offer promising physiological markers for workload estimation, existing devices are often bulky, restrictive, and susceptible to motion artifacts, limiting their practicality in real-world applications.

This study introduces a wireless, ultra-thin forehead e-tattoo that enables high-fidelity EEG and EOG monitoring while maintaining comfort, stability, and motion resistance. Unlike conventional systems, our e-tattoo leverages adhesive poly(3,4-ethylenedioxythiophene) polystyrene sulfonate (PEDOT:PSS) composite-coated electrodes to achieve low skin impedance, robust adhesion, and reliable signal acquisition during dynamic tasks. Integrated with a flexible printed circuit for on-device processing and wireless transmission, this system provides a minimally obtrusive and long-lasting solution for ambulatory cognitive monitoring. We validate the e-tattoo's capability through a dual *N*-back mental workload task, correlating EEG/EOG signals with NASA Task Load Index (NASA-TLX) self-assessments and task performance. A machine-learning model trained on these physiological features successfully estimates mental workload across varying task difficulties, demonstrating the feasibility of real-time cognitive state decoding. Our work presents a breakthrough in wearable neurotechnology, offering a scalable, cost-effective, and user-friendly approach to continuous mental workload assessment. Future applications could include real-time cognitive load monitoring in pilots, operators, and healthcare professionals, advancing the field of human-machine interaction and personalized cognitive augmentation.

SUMMARY

Real-time monitoring of operator cognitive states can enhance the safety and performance of human-in-the-loop systems. However, traditional electroencephalography (EEG) and electrooculography (EOG) devices, with their bulkiness, dangling wires, and time-consuming setups, are restricting or impossible for monitoring operators' cognitive states while performing tasks in reality. In this study, we propose a wireless forehead EEG and EOG sensor designed to be as thin and conformable to the skin as a temporary tattoo sticker, which is referred to as a forehead e-tattoo. This e-tattoo employs adhesive poly(3,4-ethylenedioxythiophene) polystyrene sulfonate (PEDOT:PSS) composite-coated graphite-deposited polyurethane (APC-GPU) electrodes laminated with a battery-powered flexible printed circuit (FPC) for data acquisition and wireless transmission. The forehead EEG and EOG measured by this e-tattoo are correlated with mental workload during a dual *N*-back working memory task. The results confirm the feasibility of applying the wireless, low-profile, forehead e-tattoo for mental workload estimation.

Please cite this article in press as: Huh et al., A wireless forehead e-tattoo for mental workload estimation, Device (2025), https://doi.org/10.1016/j.device.2025.100781

INTRODUCTION

Human mental workload is a crucial factor in the fields of human-machine interaction and ergonomics due to its direct impact on human cognitive performance. Although its definition varies, mental workload can generally be described as the degree to which a person's working memory capacity and cognitive processes are engaged by the ongoing task.[1] In addition, mental workload is closely related to other cognitive components such as engagement[2] and arousal[3] that can affect task performance. Previous research indicates that a moderate level of mental workload is essential to maintain engagement and attention, leading to optimal performance.[4] On the contrary, performance may decline when mental workload is too low or too high. At low levels of mental workload, a person can become disengaged and make mistakes. At high levels, a person may become overwhelmed and lose control. Therefore, managing users' mental workload levels is of significant interest to designers of human-in-the-loop systems to optimize performance. This becomes particularly important in high-complexity, safety-critical tasks where reductions in performance can and have resulted in devastating losses of lives and assets.[5,6] In such contexts, mental workload has been directly correlated with accident probability.[7] This has motivated various studies in mental workload assessment for operators, particularly for vehicle drivers,[8,9] aircraft pilots,[10,11] air traffic controllers,[12,13] and robot teleoperators.[14]

Although the importance of mental workload in human performance is well established, its measurement is not. It is intrinsically challenging to assess mental workload because it is a multidimensional and non-stationary variable that is determined by a combination of factors, including the inherent nature and difficulty of the task, the circumstances under which a person performs the task, as well as the skill and fatigue level of the operator at that moment.[15] Until today, NASA's Task Load Index (NASA-TLX),[16] a self-reported questionnaire, still serves as the gold standard for mental workload assessment.[15,17] However, self-assessment suffers from poor temporal resolution, intrusiveness to the ongoing task, and subjectivity.[18] Furthermore, individuals tend to report workload levels that are deemed suitable for their performance, rather than objectively reflecting their cognitive effort. Meanwhile, task performance is often observed after the task has been attempted,[15] which does not allow proactive prevention of errors or failures. This limits the usefulness of task performance as the primary measure of mental workload in safety-critical contexts that require anticipatory measures.

Physiological indices have been proposed as a promising alternative to quantifying mental workload due to their temporal resolution, high sensitivity, and neutral bias.[19,20] While easy-to-measure peripheral nervous system signals, such as heart rate[8] and electrodermal activity[21] have been associated with mental stress, these signals do not directly reflect or measure mental workload itself. EEG is the main signal modality for monitoring physiological mental workload monitoring,[13] but conventional EEG measurement systems are wired, bulky, and uncomfortable. Ocular activities such as blinks, saccades, and pupillary response have also been associated with mental workload.[22,23] Optical eye tracking is commonly used but has restrictive requirements, such as the need to fix the operator's head direction toward external sensors and the absence of optical confounders such as certain types of eyewear,[24,25] which can be unrealistic in real-world task scenarios. In contrast, EOG does not have such restrictions while recording rich blink and saccade information with high temporal resolution.[26,27] In fact, EOG has been correlated with drowsiness/fatigue,[28,29] vigilance,[30] and mental workload.[22]

Despite the desirability and demonstrated success of electrophysiology-based mental workload assessment, recording hardware has limited its widespread use. Wired recording systems not only physically restrict the user's range of movement but also suffer from significant motion artifacts, making them impractical and uncomfortable to use as mobile, wearable systems. Discomfort and restrictions on user movement also inherently modify the task environment, reducing task performance and undermining the purpose of mental workload assessment. In addition, EEG systems based on conventional gel electrodes require long setup times and suffer signal-quality degradation after a few hours due to gel drying, limiting potential applications.[31]

Recent advances in wireless wearable devices based on dry electrodes have increased the practicality of EEG. Many of them are in the form factor of a headband,[32–35] which is convenient to wear but allows relative displacement between the electrode and the skin. This compromises signal quality, especially under facial expression or body movement.[36] Emerging wearable EEG/EOG sensors in the form of glasses,[37] earbuds,[38] and headphones[39] improved wearability but suffer from similar issues of unstable electrode-skin interfaces due to stiffness mismatch between sensor and skin and non-adhesive electrodes used. Furthermore, restricting possible recording sites to peripheral locations can reduce the relevance of signals to the intended application. Such wearables are also less compatible with head-worn equipment, such as helmets for aircraft pilots, much like in the case of traditional EEG caps.

To address these issues, alternative form factors of wearable electronics such as e-tattoos have been developed for EEG and EOG.[40–46] Such systems feature stretchable and ultra-thin dry electrodes forming a conformable and stable contact with the skin. However, many EEG e-tattoos still suffer from limitations such as reliance on expensive materials or equipment,[46] tedious[45,47] and/or high-temperature[43] fabrication steps, high contact impedance with the skin,[48] lack of on-device data acquisition (DAQ),[40,44,49] or a right-leg drive (RLD)[49] for noise reduction.[50] Furthermore, despite the thinness of tattoo-like electrodes in these systems, their electronic circuits and packages, if any, still compromise overall system thinness (Table 1), making the device still obstructive to head-worn equipment such as helmets and virtual reality (VR) headsets. These limitations hinder the use of current e-tattoos as accessible solutions for the assessment of mental workload in real-world or dynamic task environments.

In this work, we present a wireless forehead EEG/EOG e-tattoo and the corresponding algorithm for the objective assessment of mental workload. We hypothesize that the e-tattoo can record high-fidelity EEG and EOG signals from the forehead that are adequate for mental workload decoding, given

Please cite this article in press as: Huh et al., A wireless forehead e-tattoo for mental workload estimation, Device (2025), https://doi.org/10.1016/j.device.2025.100781

Table 1. Comparison of forehead wearables for EEG and EOG

Reference	Channels	Application	Electrode materials	Electrode substrate	Contact impedance	System thickness	System weight	Current draw and battery life	RLD
Our work	4 EEG 2 EOG	mental workload monitoring	PEDOT:PSS-coated GPU	Tegaderm	2.1–38.7 kΩ 1.3–23.1 kΩcm^2 @ 10 Hz	117 μm (electrode) 7.5 mm (system)	4.1 g (8.1 g with battery)	5.25 mA 28.5 h @ 150 mAh	yes
40	4 EEG 2 EOG 2 EMG	sleep-stage monitoring	carbon	temporary tattoo	N/A	N/A (electrode) large[a] (system)	large[a]	N/A[a]	no
41	3 EOG	eye vergence tracking	AgNP	Ecoflex	6.3–8.4 kΩ @ 30 Hz	67 μm (electrode) N/A (system)	3.3 g (5.5 g with battery)	<105 mA 1 h @ 105 mAh	yes
42	1 EEG	error-related potential detection	gold	parylene, tattoo paper	40–50 kΩ @ 10 Hz	900 nm (electrode) large[b] (system)	8.237 g	N/A 8 h	yes
43	7 EEG	N/A (eye open vs. close test with single channel EEG only)	phase-separated PEDOT:PSS in elastomer with Ag/AgCl particles	PU	64 ± 18 kΩ @ 10 Hz	70 μm (electrode) 6 mm (system)	12 g	22.9 mA[c] 8.73 h 200 mAh	no
44	4 EEG 3 EOG 1 EMG	N/A (eye open vs. close test)	Ag-In-Ga-SIS	TPU	69.9 kΩ @ 100 Hz	210 μm (electrode) 10 mm (system)	8 g (13.99 g with circuit)	<50 mA	yes
45	2 EEG 2 EOG 1 EMG	sleep-stage monitoring	gold	PTFE, Ecoflex, Silbione, fabric, etc.	5 kΩcm^2 @ 30 Hz	250 μm (electrode) N/A (system)	N/A	14.2mA + 9.2mA 10.56 h @ 150 mAh	yes

Units for contact impedance vary depending on availability of area-normalized contact impedance. RLD, right-leg drive; N/A, not applicable.
[a]Connects to a commercial amplifier/data acquisition box.
[b]Connects to a rigid PCB with 3D printed encapsulation.
[c]Reported in their prior work.[49]

CellPress

Please cite this article in press as: Huh et al., A wireless forehead e-tattoo for mental workload estimation, Device (2025), https://doi.org/10.1016/j.device.2025.100781

prior investigations on the neural correlates of mental workload and its decoding.[9,51,52] Instead of using thin noble-metal films as electrodes and interconnects, we adopt the cut-and-paste method[53] to fabricate stretchable serpentine ribbons from commercially available conductive graphite-deposited polyurethane (GPU) sheets. To reduce the contact impedance of GPU and improve attachment to human skin, we create an adhesive PEDOT:PSS composite (APC) coating on GPU filamentary serpentines for forehead EEG and EOG measurements with suppressed motion artifacts. We demonstrate the thinness, conformability, stretchability, adhesiveness, conductivity, and manufacturability of APC-GPU electrodes. We design a flexible printed circuit (FPC) with an RLD circuit that transmits low-noise EEG and EOG data in real-time via Bluetooth Low Energy (BLE) while achieving the lowest power consumption among similar reported wireless flexible EEG sensors. We also use the high-fidelity EEG and EOG signals recorded with our device to train and evaluate random forest models for mental workload evaluation, without the need for extensive offline signal processing steps. Our hardware-software system is an all-in-one user-friendly solution for decoding mental workload, with a thin form factor compatible with other headgears (Figure S1). Its capability is demonstrated by successfully estimating mental workload levels in six human subjects performing a dual *N*-back task with the ground truth of mental workload provided by both task performance and NASA-TLX self-assessment.

RESULTS

Wireless forehead e-tattoo design

Figures 1A–1E present front, side, and close-up views of our wireless forehead e-tattoo. It records four channels of EEG (AF7, Fp1, Fp2, AF8) on the forehead and two channels of EOG across the eyes (vertical EOG, horizontal EOG). The e-tattoo comprises a disposable tattoo-like electrode layer and a reusable FPC layer. As the electrode layer must cover the entire forehead, it is designed with filamentary serpentine-shaped electrodes and interconnects made of commercially available low-cost, conductive GPU, compared to expensive gold thin films. Cut-and-paste approach[53] enables the time- and cost-effective fabrication of the filamentary serpentine GPU on a transparent Tegaderm tape (see methods). An APC is developed to coat only the electrode regions of the GPU to reduce the contact impedance and enhance the adhesion to the skin. The FPC for data acquisition and wireless data transmission (Figure 1F) is designed with a two-layer circuit of thickness 117 μm to achieve a footprint of 8.58 cm^2 and a total weight of 8.1 g including a 150-mAh battery. The island-serpentine structural design[54] increases the stretchability and flexibility of the FPC, allowing it to accommodate facial expressions. The FPC stacks on top of the Tegaderm-supported GPU electrode layer and connects to the electrodes through *z* axis conductive anisotropic cohesive films (ACFs) (Figure S2). This simple FPC-to-electrode via connection works due to the double-sided conductivity and the thickness of the GPU interconnects (50 μm).[55] The fully assembled wireless sensor conforms to and stays attached to the forehead without mechanical perception to the user. Only the electrode layer directly contacts the skin and therefore should be disposed after use. The ACF allows easy disassembly of the FPC from the electrode layer, allowing the disposal of the electrode layer and the reuse of the FPC with a new electrode layer.[56] Our system stands out in comparison with previously reported forehead EEG and EOG sensing systems, as summarized in Table 1, particularly excelling in terms of low contact impedance and current draw, making it highly suitable for long-term mental workload-monitoring applications. The following results validate the capability of the wireless forehead e-tattoo and demonstrate mental-work assessment from prefrontal EEG and EOG during dual *N*-back task (Figure 1G).

Figure 2 presents the composition as well as the mechanical and electrical properties of the APC-GPU electrodes. As a large-area, disposable e-tattoo is required for EEG and EOG acquisition over the forehead, GPU provides a cost-effective solution, with an estimated cost of less than $20 for each tattoo. However, unlike conventional gold-nanomembrane-based filamentary serpentines,[45,47] which can self-conform to skin microtopography without added adhesive, 50-μm-thick commercial GPU cannot form microscale conformability to skin[57] even with filamentary serpentine patterns and adhesion provided by the supporting Tegaderm tape. As a result, the filamentary serpentines of the bare GPU suffer from high contact impedance and susceptibility to relative motion with the skin. To address these issues, we have adapted an APC to coat the GPU electrodes (but not the GPU interconnects). The APC, first introduced by Tan et al.,[58] consists of PEDOT:PSS, β-cyclodextrin, citric acid, and glutaraldehyde-crosslinked polyvinyl alcohol (PVA) to achieve low modulus, high stretchability, and stable interface adhesion (Figure 2A). It is well known that the ionic conductivity[59] and the self-adhesiveness[60] of PEDOT:PSS can both significantly reduce contact impedance with the skin. Although the APC is not our original development, we have optimized its composition for the GPU electrode coating, which effectively improves both adhesion and EEG sensing from the skin.

A cross-sectional view of a scanning electron microscopy (SEM) image shows that APC can be uniformly blade-coated and dries on GPU, resulting in a 30 ± 4-μm-thick layer (Figure 2B). The surface profiles of the electrodes before and after APC coating are compared in Figure S3. APC coating decreased the average surface roughness (Sa) from 0.527 to 0.421 μm. The supramolecules formed by β-cyclodextrin and citric acid in APC can enhance the hydrogen bonding between the APC and the surface of the skin, which is covered by stratum corneum consisting of keratin and lipids,[61,62] enabling conformal and stable contact of the electrode on the skin (Figures 2C and S4).

Additionally, the PEDOT:PSS content of the APC-GPU electrodes can be tuned to balance softness and conductivity. Due to the relatively high stiffness (Young's modulus, $E > 500$ MPa) and the small strain to failure of PEDOT:PSS (2%),[63] increasing the mass ratio of PEDOT:PSS in the APC enhances conductivity but compromises the softness and stretchability of the electrodes. Therefore, we compared the mechanical properties of the GPU and APC-GPU with PEDOT:PSS mass ratios of 1.8%, 3.6%, 7.1%, 13.2%, and 23.3% in the APC. As shown in Figure 2D, the fracture strain decreased from 138% for 1.8% APC-GPU to 82% for 23.3% APC-GPU, while the effective

Please cite this article in press as: Huh et al., A wireless forehead e-tattoo for mental workload estimation, Device (2025), https://doi.org/10.1016/j.device.2025.100781

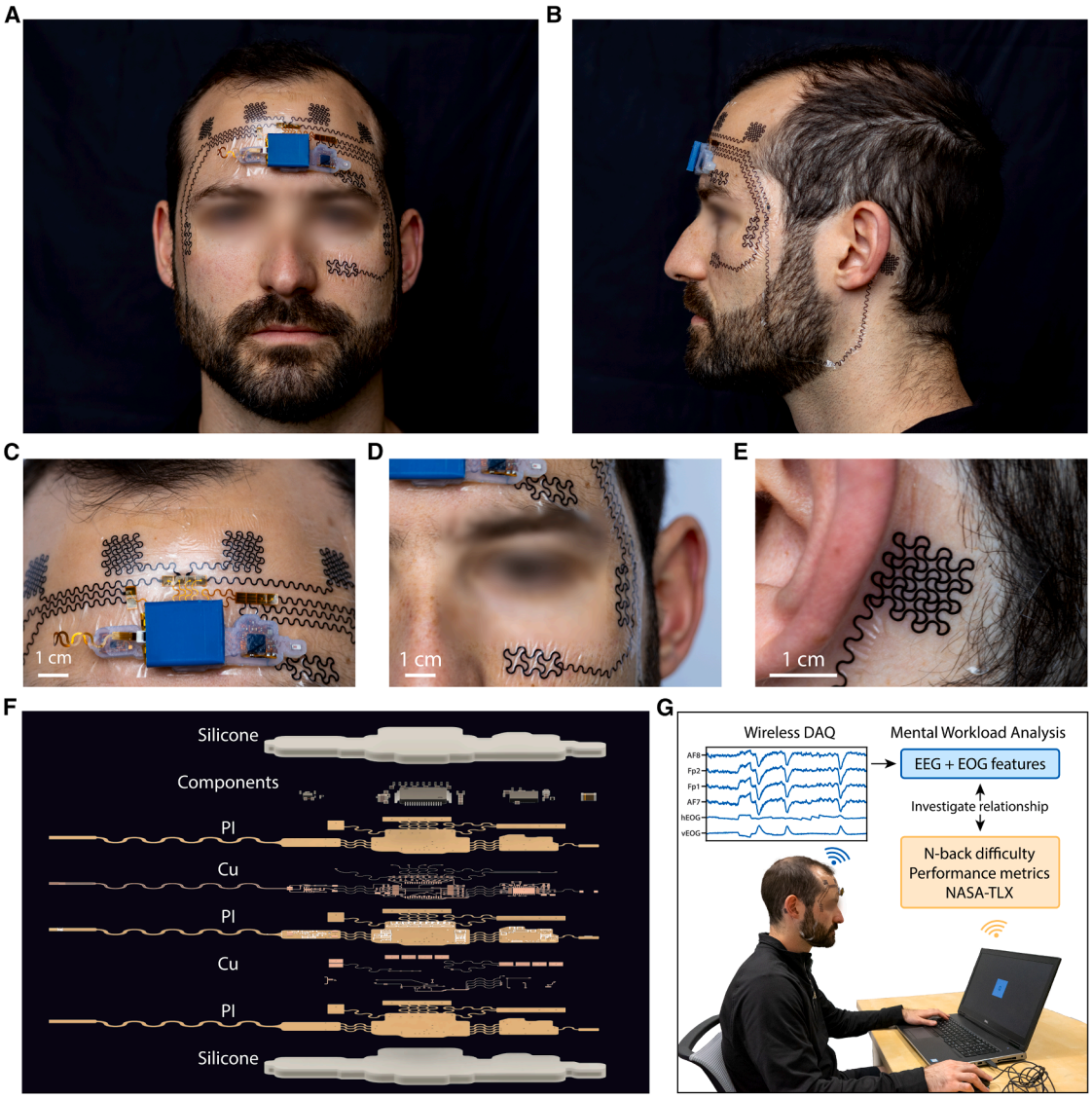

Figure 1. Wireless forehead EEG and EOG e-tattoo

(A and B) (A) Front- and (B) side-view photos of the e-tattoo worn on the forehead of a participant.

(C) Stretchable EEG electrodes laminated with encapsulated flexible printed circuit (FPC) on the forehead.

(D) Three e-tattoo electrodes for EOG.

(E) Reference or ground e-tattoo electrode attached to the mastoid.

(F) Exploded view of the multilayer FPC. The island-serpentine-bridge design and the soft silicone encapsulation increase the stretchability and conformability of the FPC.

(G) Experimental setup for mental workload monitoring while taking the dual *N*-back task. The wireless forehead e-tattoo captures real-time EEG and EOG signals. The relationships between extracted physiological features and behavioral performance metrics were thoroughly analyzed.

Young's modulus increased from 108 MPa to 147 MPa. Figure 2E shows that APC-GPU with a PEDOT:PSS mass ratio of 3.6% has the strongest adhesion of 80 N/m, while the APC-GPU with PEDOT:PSS concentration of 23.3% has the weakest adhesion of 10 N/m. In particular, the APC-GPU exhibited an adhesion force 12 times larger than that of the commercial liquid gel EEG electrode (6 N/m), suggesting its higher stability under motion. Furthermore, Figure S5 shows that the APC layer with 3.6% PEDOT:PSS functions as both an adhesive and a mechanically compatible interface, achieving perfect conformability to the skin even in the absence of an adhesive substrate. In contrast, bare GPU cannot fully conform to the skin even if supported by an adhesive Tegaderm substrate. Thus, results show that APC-GPU is clearly superior to GPU and gel electrode in adhesion.

In terms of electrical properties, the sheet resistances of bare GPU and APC-GPU are nearly identical, around 50 Ω/sq (Figure 2F). This suggests that the thin APC has little effect on

Please cite this article in press as: Huh et al., A wireless forehead e-tattoo for mental workload estimation, Device (2025), https://doi.org/10.1016/j.device.2025.100781

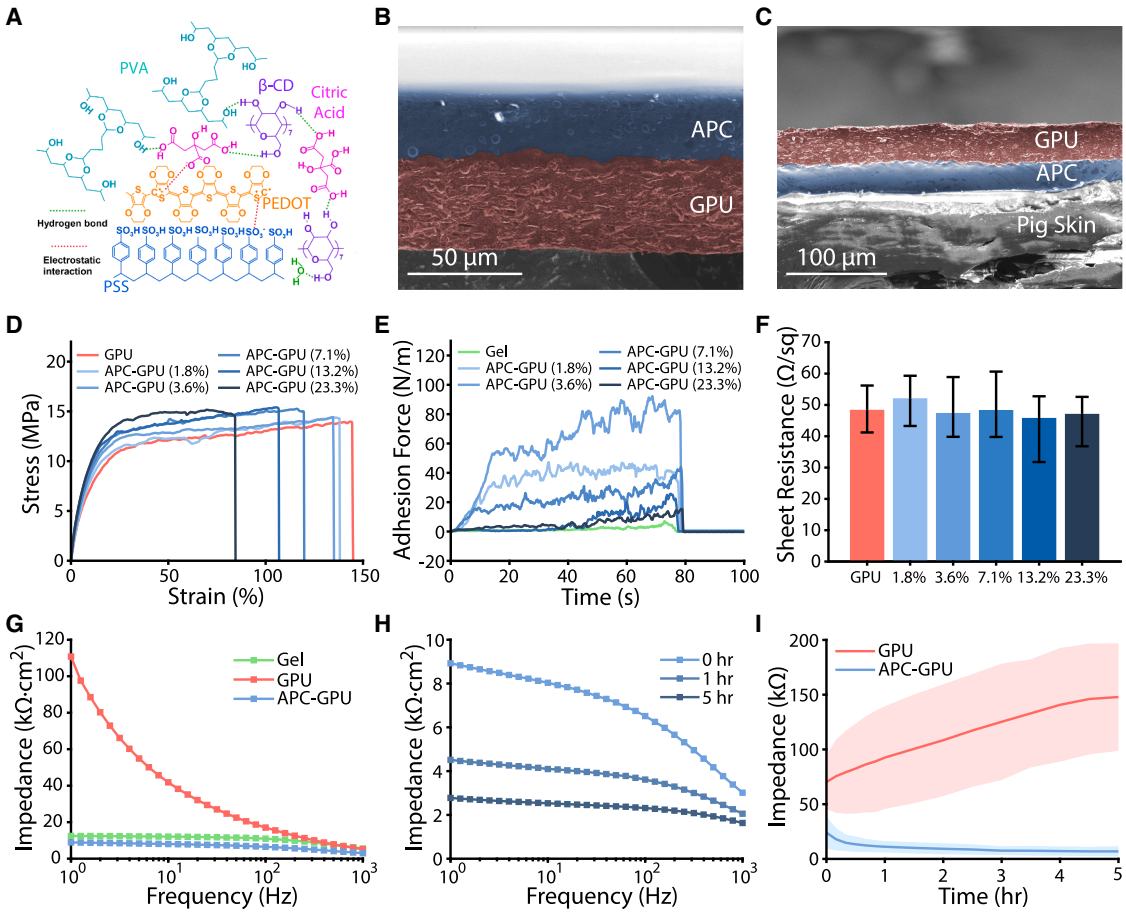

Figure 2. APC-GPU electrodes

(A) Molecular structures and interactions of the chemical components in the APC, including PEDOT, PSS, citric acid, polyvinyl alcohol (PVA), and β-cyclodextrin (β-CD).

(B) Cross-sectional SEM image showing conformable coating of APC on GPU.

(C) Cross-sectional SEM image showing APC-GPU electrode seamlessly adhering to the pig skin due to the APC coating.

(D) Stress-strain curves of GPU and APC-GPU films with various PEDOT:PSS mass ratios (1.8%, 3.6%, 7.1%, 13.2%, and 22.3%).

(E) Comparison of the skin adhesion forces of gel and APC-GPU films measured by the 90° peel test.

(F) Sheet resistance of the GPU and APC-GPU films.

(G) Area-specific skin contact impedance of conventional gel electrode and APC-GPU electrodes (with PEDOT:PSS mass ratio of 3.6%) right after application.

(H) Area-specific skin-electrode contact impedance sweep of the APC-GPU electrode at 0, 1, and 5 h after application.

(I) Change in average contact impedance of bare GPU and APC-GPU electrodes on human skin over 5 h with confidence interval set at 95% (shadowed area).

the overall resistance of the GPU because the GPU is more electrically conductive than the thin APC layer, whose sheet resistance was measured to be 68.34 ± 38.12 Ω/sq. Therefore, uncoated GPU serpentine ribbons served as stretchable, low-resistance interconnects, which are also low cost and easy to manufacture. Although APC coating does not affect the sheet resistance of GPU, it can significantly reduce contact impedance with the skin due to the simultaneous electrical and ionic conductivity of PEDOT:PSS, which can facilitate the conversion of ionic current to electronic current.[59] The contact impedance of the APC-GPU electrode at different PEDOT:PSS mass ratios is presented in Figure S6, showing that APC-GPU outperforms gel-based electrodes, with a PEDOT:PSS mass ratio of 3.6% showing the lowest contact impedance. Given its high stretchability, strong adhesion, and low contact impedance, APC-GPU with a 3.6% PEDOT:PSS mass ratio was used in all the following experiments.

To further evaluate the performance of APC-GPU under dynamic conditions, impedance hysteresis and cyclic loading tests were conducted up to 30% strain.[64] The impedance responses during loading and unloading are presented in Figure S7, showing that impedance variations remained within 300 Ω, with a hysteresis of 59 Ω. Additionally, Figure S8 illustrates impedance changes over 1,800 cycles, where the impedance stabilized after 500 cycles, remaining between 0.86 kΩ and 1 kΩ.

Figure 2G compares the contact impedance of the APC-GPU electrodes with that of the bare GPU electrodes and the gel electrodes (Kendall disposable surface electrode, USA). APC-GPU electrode achieved a remarkably low contact impedance of 8.03 kΩ · cm^2 at 10 Hz, which was even lower than that of the

Please cite this article in press as: Huh et al., A wireless forehead e-tattoo for mental workload estimation, Device (2025), https://doi.org/10.1016/j.device.2025.100781

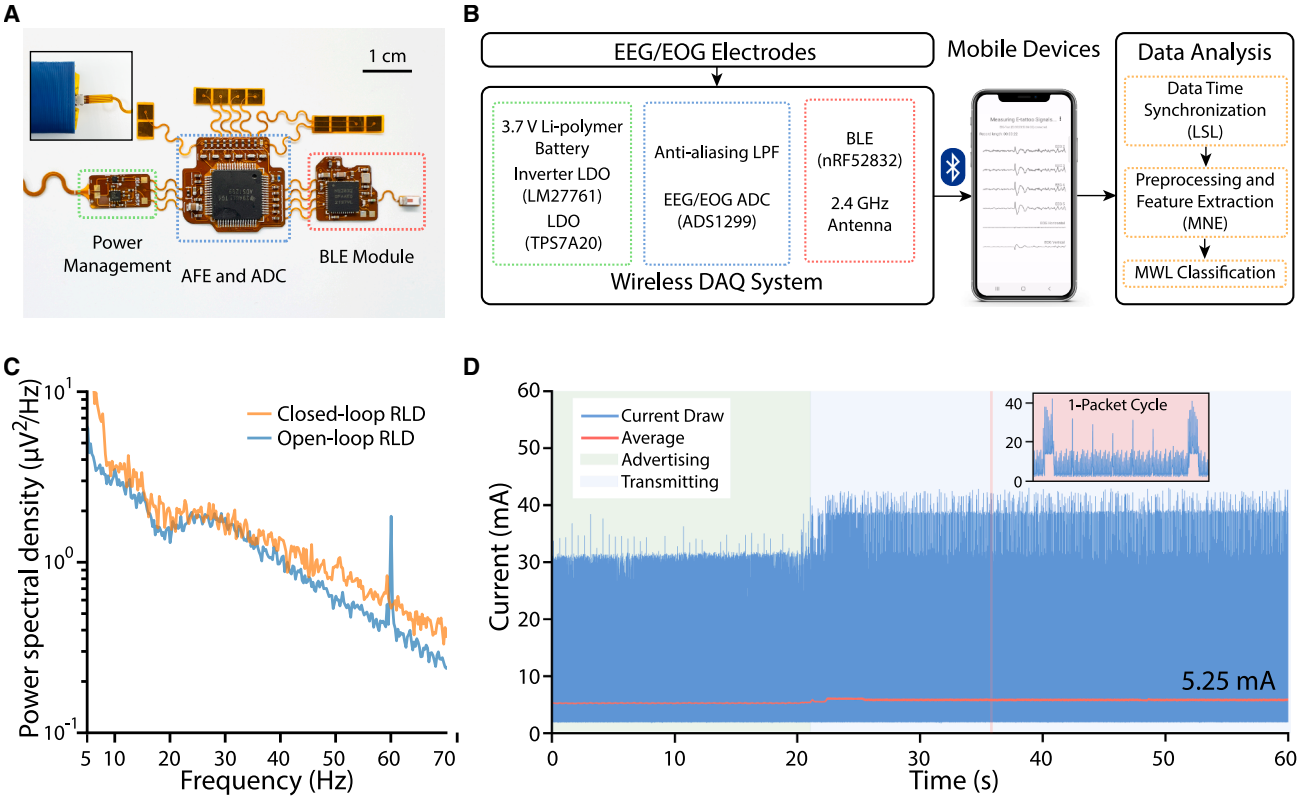

Figure 3. Design of the FPC

(A) Photo of the FPC consisting of a power-management module, an analog front-end (AFE) and analog-to-digital converter (ADC) module, and a Bluetooth (BLE) module. The inset shows the FPC serpentine extension connecting to a rechargeable LiPo battery.

(B) Block diagrams of the FPC and the workload-estimation pipeline.

(C) Comparison of EEG power spectra between closed-loop and open-loop RLD implementations in the presence of 60-Hz powerline noise.

(D) Current draw of the e-tattoo under normal advertising and data-transmitting periods over 60 s. The inset shows instantaneous current draw in between two packet transmissions (40-ms period).

commercial gel electrode (12.06 kΩ · cm^2). The contact impedance of the APC-GPU electrode decreased over time in a typical EEG bandwidth of 1–100 Hz as shown in Figure 2H. At 10 Hz, the contact impedance of the APC-GPU electrode gradually decreased from 8.03 kΩ · cm^2 to 2.53 kΩ · cm^2 after 5 h due to slight sweat secretion. The reduction in contact impedance after exercise (Figure S9) further confirmed the effect of sweat on reducing the contact impedance. Despite excessive sweating during exercise, the adhesion of the APC-GPU is still sufficient to maintain good contact with the skin, which is important for monitoring EEG under dynamic motion. Figure 2I shows that the average contact impedance of APC-GPU electrodes always remained under 25 kΩ during the test period, ensuring high EEG and EOG signal quality. In contrast, the contact impedance of the bare GPU electrodes increased with time as sweat plays little role with non-ionically conductive GPU but sebum secretion worsened the mechanical and electrical contacts between the electrode and the skin. In conclusion, the APC coating significantly enhances the performance of GPU-based filamentary serpentine electrodes by improving adhesion and reducing electrode-skin contact impedance. These innovations ensure reliable, high-quality EEG and EOG signal acquisition even under dynamic movements, making APC-GPU electrodes a promising solution for large-area, accessible, and disposable forehead e-tattoos.

We custom designed an FPC (Figure 3A) for low-power, high-fidelity EEG/EOG data acquisition and wireless transmission. The exploded view of the double-layer FPC is offered in Figure 1F. The island-serpentine-bridge design provides both mechanical isolation to rigid IC chips to maximize conformability to the curved forehead and electrical isolation between power, analog, and digital modules to improve circuit stability. The total FPC footprint is only 858.37 mm^2. The power-management module has a serpentine extension that can simply slide into a low-profile FPC connector mounted on a small rechargeable lithium polymer (LiPo) battery (Figure 3A, inset). The central analog front-end island is connected to three signal-input terminals containing 10 copper pads (four EEG electrodes, one common EEG reference electrode, one RLD ground electrode, and four EOG electrodes forming two bipolar channels). The copper pads on the FPC layer are connected to the GPU terminals in the e-tattoo layer via ACF tape. Figure 3B offers a block diagram of the wireless forehead e-tattoo system. The EEG and EOG signals are low-pass filtered (LPF) for antialiasing and then amplified

Please cite this article in press as: Huh et al., A wireless forehead e-tattoo for mental workload estimation, Device (2025), https://doi.org/10.1016/j.device.2025.100781

and converted to digital signals by a 24-bit analog-to-digital converter (ADC; Texas Instruments ADS1299). For EEG data acquisition, closed-loop RLD configuration (Figure S10A) was implemented after comparing its stability and common mode rejection ratio with other popular configurations in an SPICE simulation (Figure S10B). This configuration achieved an 85.7% reduction in the body-coupled 60-Hz powerline noise (Figure 3C) compared to the open-loop alternatives. Powerline contaminations are ubiquitous in ambulatory settings. The ADS1299 communicates via a serial peripheral interface (SPI) with the Nordic nRF52832 BLE system on a chip, which was programmed via a serial wire debug (SWD) interface. A custom Android application marks every wirelessly acquired sample with a unique timestamp based on the Lab Streaming Layer architecture.[65] This allowed the EEG and EOG data to be temporally synchronized with each other and with external data or event timing information such as in our dual *N*-back task study. The stability of the wireless transmission was characterized by the low mean packet loss of 0.07% at distances below 1 m and 0.5% at distances below 10 m (Figure S11). Overall, the data acquisition system had several favorable performance characteristics such as low self-noise of 0.079 μVrms and 0.634 μVpp, as shown in Figures S12A and S12B. Additionally, it had a low-noise corner frequency of 10^{-1} Hz (Figure S12C), which is well below the frequencies of interest in EEG and EOG signals. The accuracy of the physiological signals collected by our device is demonstrated through comparisons with a gold-standard device, as described in the next section. Given our system average current draw of 5.25 mA (5.23 mA in advertising phase, 5.26 mA in active data transmission) (Figure 3D), a 3.7-V, 150-mAh LiPo battery (which was seamlessly integrated into the device via a modified connector; see Methods for details) can last more than 28 h without interruption. The current draw was measured in the recording configuration used for all measurements in the study (closed-loop RLD enabled, sampling rate = 250 Hz, 25 packets transmitted per second, 10 six-channel data samples per packet). Table 1 highlights the low power consumption and long-term operation when comparing our device with existing wireless forehead EEG systems.

Signal-quality validation

We adopted a commercially available, widely used wireless EEG system, the Brain Vision actiCAP active electrodes with LiveAmp 32 amplifier (Brain Products, Germany), as the gold standard for the validation of our signal quality. Figure 4 compares the signal quality and motion artifacts between the two. All EEG electrodes were applied to AF7, Fp1, Fp2, and AF8. In this comparison, solid gel-based active electrodes (actiCAP, Brain Products, Germany) were placed right above the APC-GPU electrodes with an offset of 1 cm. The reference and ground electrodes were also placed adjacent to each other on the mastoids. The gel electrodes were connected to the LiveAmp amplifier through standard DIN 1.5-mm EEG cables. The Brain Vision system and the forehead e-tattoo were configured to record signals simultaneously at a sampling rate of 250 Hz.

To assess the ability of the forehead e-tattoo to record basic neural activities, we measured the synchronization and desynchronization of the alpha EEG band (8–12 Hz) during open and closed eyes. Alpha synchronization (i.e., elevated EEG alpha band power) is expected when eyes are closed.[66] Alpha band-pass-filtered EEG signals from both the Brain Vision system (Figure 4A) and the forehead e-tattoo (Figure 4C) indicated similar levels of alpha activity during closed and open eyes. Similarly, Figures 4B and 4D show the average spectrograms across all four EEG channels obtained by the Brain Vision system and the e-tattoo, respectively. The EEG signals and the average spectrograms are virtually indistinguishable, validating the EEG sensing capabilities of the wireless e-tattoo. Figure S13 also shows that our e-tattoo captured the apparent alpha synchronization during eye closing in all subjects. By accurately measuring the visual stimuli-modulated changes in alpha activity, we validated the feasibility of using the e-tattoo for applications requiring accurate neural spectra information.

Our e-tattoo also clearly distinguishes horizontal EOG (hEOG) and vertical EOG (vEOG) during eye movements and blinks (Figure 4E). During vertical eye movements, there was a lack of hEOG signals and vice versa, which can be attributed to the precise placement of the hEOG and vEOG electrodes owing to the high customizability of the e-tattoo to fit an individual user's face. Distinctive orthogonal EOG measurements enable a wider range of EOG analysis than combined EOG measurements in other wearable platforms.[67,68] Weak and strong blinks were also captured accurately by the e-tattoo as evident in the vEOG channel. They are important for regression-based EOG artifact removal from the forehead EEG signals.

Many motion artifact removal methods for ambulatory EEG rely on a considerable number of EEG channels, which can be impractical for wearable form factors.[69,70] Additionally, these approaches often incorporate external sensing modalities, such as accelerometers, which can add complexity to the system. On the other hand, a significant advantage of cable-free wireless EEG sensing is suppression of motion artifacts without extensive signal processing. Figure 4F compares the EEG measured by the Brain Vision system (red) and the forehead e-tattoo (blue) during head rotations (looking up/down/left/right), facial muscle movements (raising eyebrows, smiling, swallowing), and outdoor activities (walking and running). EEG signals recorded by the Brain Vision system were significantly corrupted by dynamic movements such as head rotations, walking, and running, while the e-tattoo EEG remained unaffected. Figure S14 shows that the average root-mean-square (RMS) values of the EEG signals under different motion conditions were 1,847.26 and 68.04 μV for the Brain Vision and forehead e-tattoo, respectively. The RMS value of the forehead e-tattoo EEG falls within the typical EEG amplitude range of 10–100 μV. Only during eyebrow raising did the e-tattoo EEG fluctuate more than the Brain Vision EEG due to the relative proximity of the e-tattoo electrodes to the eyebrows. Other subtle facial expressions, such as smiling and swallowing, did not induce significant motion artifacts in either system. The relative immunity to motion artifacts indicates that the wireless forehead e-tattoo holds promise for real-life mental workload monitoring.

Dual *N*-back task design and behavioral analysis

The *N*-back task has been widely adopted to parametrically evoke different levels of working memory load by adjusting the

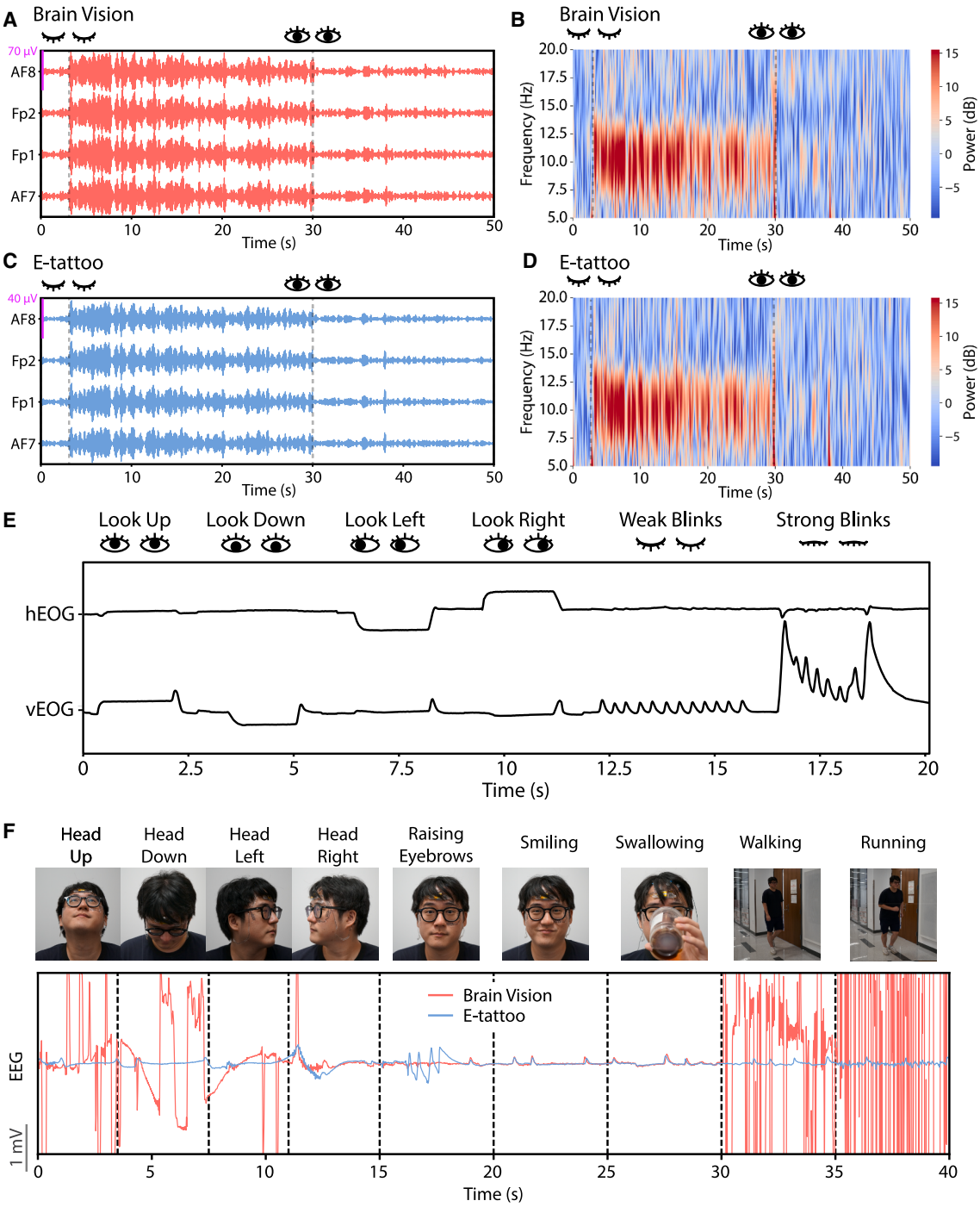

Figure 4. Signal quality validation against Brain Vision EEG device using gel electrodes

(A–D) Alpha band-filtered EEG and spectrograms from (A and B) Brain Vision and (C and D) forehead e-tattoo simultaneously measured during eye open-closed test.

(E) Horizontal and vertical EOG measured from forehead e-tattoo under various eye movements and blinks.

(F) Brain Vision (red) and e-tattoo (light blue) measured EEG under various head movements, facial expressions, and ambulatory movements.

N value, directly taxing the prefrontal cortex, which is a key brain region associated with cognitive control and mental effort.[52,71] We, therefore, designed a dual *N*-back task in which the subjects need to memorize a sequence of the stimuli: the positions of the cells shown and the alphabet characters within them. It is called dual *N*-back task because it forces the subject to maintain a

Please cite this article in press as: Huh et al., A wireless forehead e-tattoo for mental workload estimation, Device (2025), https://doi.org/10.1016/j.device.2025.100781

constantly updating short-term working memory of two different pieces of information: alphabet (visual) and cell position (spatial). The visuospatial trial's difficulty level escalates as the load factor *N* increases from 0-back to 3-back. Figure 5A illustrates our experimental paradigm and the sequence of our dual *N*-back task. Each experimental session comprises three runs with 5-min breaks between them. Within each run, 16 *N*-back trials are evenly distributed across four difficulty levels (0-, 1-, 2-, and 3-back) in randomized order. During each *N*-back trial, subjects are presented with 20 stimuli, each consisting of a visual display of an alphabet character inside a highlighted cell lasting 0.6 s, followed by a black screen for 1.4 s, totaling 2.0 s per stimulus. When a stimulus is repeated either in cell position or character *N* stimuli after its previous appearance, subjects need to respond by clicking a mouse button (left for a character match, right for a position match). In the 0-back scenario, subjects are pre-assigned a target character and a cell position before the stimulus cycle begins. After each run, subjects were asked to evaluate their task load and performance using the NASA-TLX questionnaire.

Under Institutional Review Board (IRB) approval, we recruited six healthy adults to perform the aforementioned dual *N*-back task. We examined NASA-TLX ratings, behavioral performance, and physiological indices together to analyze the effects of *N* and to validate that the *N*-back task design can successfully induce mental workload that increases with *N*. Figure 5B shows that the averaged self-assessed total TLX increased with task difficulty, indicating statistically significant perceived difficulty levels between $N = 1, 2, 3$ with $p < 0.001$. However, the difference in total TLX between 0-back and 1-back did not achieve statistical significance at $\alpha = 0.05$ ($p = 0.053$). The average NASA-TLX ratings for six subjective subscales shown in Figure S15 indicate that increasing *N* from $N = 0$ to $N = 1$ did not increase the physical demand to accomplish the tasks, allowing us to correlate our downstream analysis of EEG and EOG features with mental workload, not physical workload. We also examined the accuracy and response time to assess subjects' behavioral performance differences between the *N* levels, which are also used as indicators to characterize changes in mental workload in earlier works.[72] Figure 5C compares the average *N*-back performance assessed by the normalized performance subscale of TLX (100 − TLX performance rating/100) and task accuracy. Both metrics showed that performance decreased as the difficulty level *N* increased. However, *N*-back performance cannot be solely represented by a single metric such as stimuli response accuracy due to different mental priorities adopted by each subject and the nature of the *N*-back task. For instance, subjects may focus on correctly identifying the matching stimuli more than correctly ignoring non-matching stimuli, or vice versa, although they were not rewarded either way. Other subjects may focus on responding to a stimulus quickly. Therefore, it is typical to evaluate *N*-back performance through an array of performance metrics. We evaluated the effects of *N*-back difficulty on average detection rates, false-alarm rates, and reaction times for correct responses, which are shown in Figure 5D. As expected, in addition to decreases in accuracy and detection rate, false-alarm rate increased with *N*. In addition, subjects reacted faster to stimuli at lower difficulties on average, although there were no incentives or penalties based on reaction time. This trend is consistent with the observations made in prior work.[73] Interestingly, although the total TLX for 1-back was not significantly higher than that of 0-back (Figure 5B), behavioral performance metrics indicated a difference (Figures 5C and 5D). Starting from 1-back, the total TLX ratings were significantly higher as *N* increased (Figure 5B), and the behavioral performance, especially the detection rate, is inversely correlated with this. In contrast, behavioral performance in terms of task accuracy, reaction time, and false-alarm rate had already plateaued at 2-back and did not worsen significantly at 3-back (Figures 5B, 5C, and 5D). These observations suggest that *N* represents the overall evoked mental workload that can be described by not one but a combination of metrics, some of which may become less or more relevant depending on the *N* level in question and presumably the nature of the *N*-back task. This result is consistent with the general understanding that each of these metrics, including NASA-TLX, covers different aspects of mental workload and its effects, as briefly explored in the Introduction. However, these are not the focus of this research and hence not fully studied. In summary, varying *N* from 0 to 3 in our *N*-back task had successfully evoked differential levels of mental workload experienced by subjects, as characterized by their NASA-TLX ratings, task accuracy, detection rate, false-alarm rate, and reaction time.

Forehead EEG and EOG features relevant to mental workload

We analyzed the EEG and EOG signals collected on six subjects using our wireless forehead e-tattoo during the dual *N*-back tasks. EEG band powers for delta (1–4 Hz), theta (4–8 Hz), alpha (8–12 Hz), beta (12–30 Hz), and gamma (30–50 Hz) bands were extracted. These measures were calculated from flattened power spectra to account for the aperiodic EEG activities across trials and subjects. In addition to EEG band powers, we also examined their various combinations, such as the beta/(alpha + theta) ratio, which is known as the engagement index.[74] EOG features we extracted include the number of eye blinks and saccades, the average blink peak (ABP), the average blink duration (ABD), and the average saccade duration (ASD). The signal-processing and feature-extraction procedures are described in detail in the Methods section and Figure S16. The correlation matrix among EEG band powers and EOG features is offered in Figure S17.

Figure 5E plots the averaged physiological features based on the *N* level. When *N* increased, frontal delta- and theta-band powers increased while alpha-, beta-, and gamma-band powers decreased. These correlations between mental workload and EEG band powers are in line with the following neuroscience studies. An increase in theta-band power has been associated with an increase in working memory load[9,51,75,76] and was most clearly observed in the frontal brain region. Increasing mental workload has been associated with a decrease in alpha power[77,78] and an increase in frontal theta power.[51,79] Importantly, increased memory load during visual information maintenance has been associated with decreases in beta power,[80,81] which is highly relevant for visuospatially evoked mental workload in our study. The beta/(alpha + theta) ratio decreased as

Please cite this article in press as: Huh et al., A wireless forehead e-tattoo for mental workload estimation, Device (2025), https://doi.org/10.1016/j.device.2025.100781

CellPress

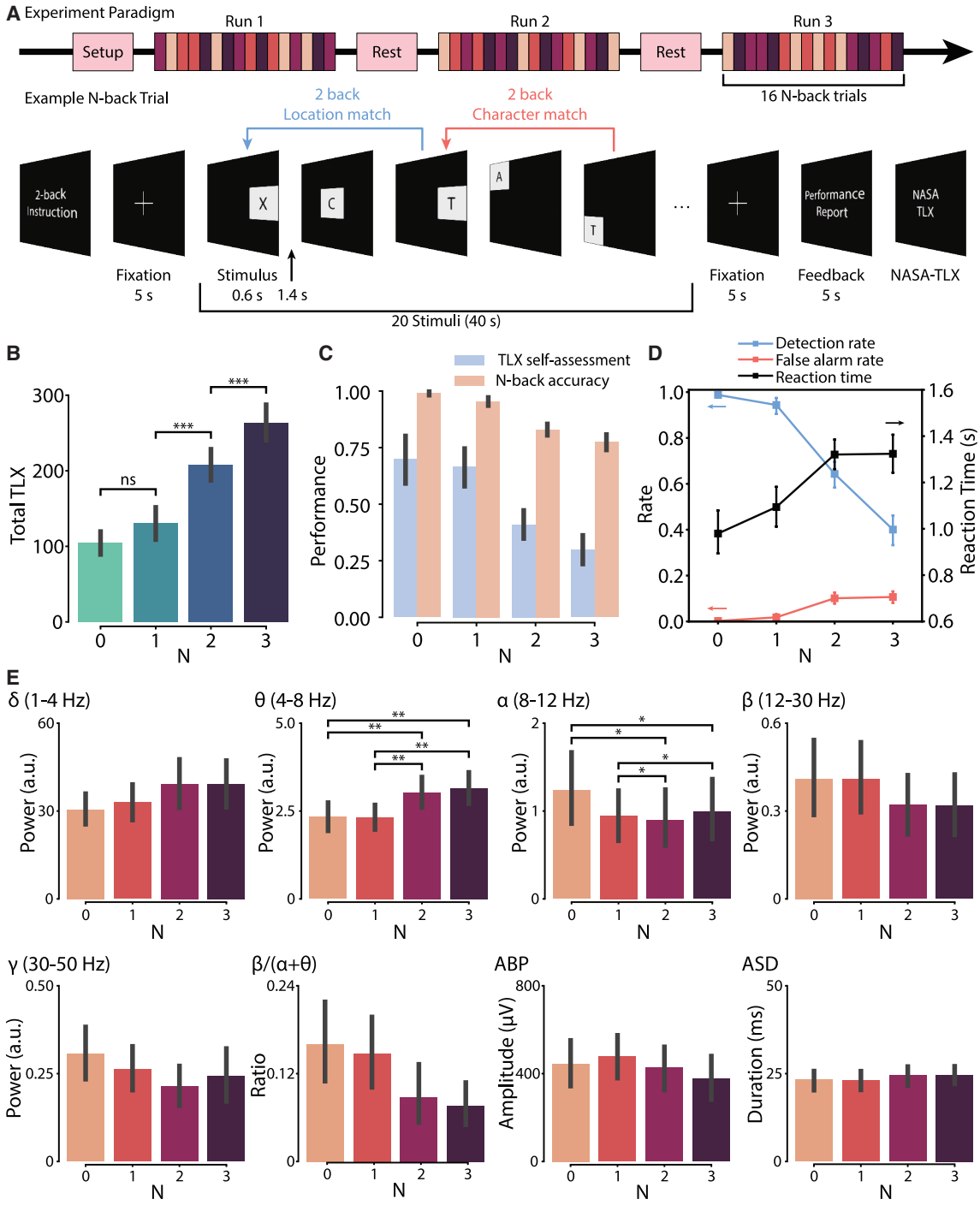

Figure 5. Dual *N*-back experiment paradigm and result analysis

(A) Diagrams of the experiment paradigm and dual *N*-back trial design.

(B) Average total NASA-TLX ratings across all trials/subjects. Perceived difficulty differs significantly between $N = 1$, 2, and 3, but not between $N = 0$ and 1 ($p = 0.0503$).

(C) Comparison of TLX-based self-assessed performance and *N*-back task accuracy.

(D) Average behavioral performances, including detection rate (blue), false-alarm rate (red), and reaction time (black), were observed across all trials and subjects changing with the *N* level.

(E) Average EEG band powers and EOG features (ABP and ASD) across *N* levels, with statistically significant differences marked ($p < 0.05$). Error bars indicate 95% bootstrap confidence intervals. Significance was tested using two-sided Mann-Whitney U tests. Ns, $p \geq 0.05$; *$p < 0.05$; **$p < 0.01$; ***$p < 0.001$.

Please cite this article in press as: Huh et al., A wireless forehead e-tattoo for mental workload estimation, Device (2025), https://doi.org/10.1016/j.device.2025.100781

N increased, which indicates that states of disengagement and low attention correlate with increased mental workload.[74,82] In our case, EOG features such as ABP and ASD did not show a strong correlation with *N*, despite the relevance of eye activity to mental workload suggested in literature.[22] This result is corroborated by some studies in which EOG measures of such activity could not be used to distinguish between levels of mental workload.[39,83]

Among all features, frontal theta ($p < 0.01$) and alpha ($p < 0.05$) band powers were significantly different between low (0- and 1-back) and high (2- and 3-back) mental workload conditions. Unlike NASA-TLX ratings, which increased gradually with *N*, the physiological features did not show a consistent trend with *N*, as each reflects different aspects of cognitive processes and mental workload. However, there were similarities between behavioral performance and physiological features. For instance, delta, theta, and beta powers and ASD plateaued after 2-back, similar to false-alarm rate and reaction time. Additionally, the engagement index, the beta/(alpha + theta) ratio, showed a similar decrease as *N* increased. These findings further support using physiological sensing alongside other metrics to develop an objective means for workload estimation.

Estimating mental workload based on forehead EEG and EOG

To evaluate the viability of mental workload estimation using the e-tattoo, we built a random forest model to predict the level of mental workload experienced by subjects during *N*-back tasks. We chose to use random forests for its robustness against overfitting and its non-parametric nature, which allows for easy application across different subjects without explicit calibration. In addition, the random forest framework has native support for both classification and regression, which we utilize in our model evaluation approach. For this evaluation, we used the known *N* label as the ground truth for mental workload. Figure 6A shows the structure of the entire dataset recorded during this study, which was divided into either 16 epochs of 40 s for trial-level regression or further divided into 16×20 epochs of 2 s for stimulus-level classification (see Methods). Figure 6B shows the confusion matrix of the stimulus-level classification summed across all subjects. To verify that the mental workload classifier achieved above-chance accuracy (1) for every subject and (2) for every *N* level, we plotted the micro-averaged one-versus-rest (OvR) receiver operating characteristic (ROC) curves of each subject and compared them to that of a random unskilled classifier (Figure 6C). We found that the model can successfully estimate the mental workload for all *N* levels for all six subjects. Finally, to validate mental workload estimation of a given subject over time, we performed trial-level regression of *N* using a random forest regression model. Figure 6D shows the 3-fold cross-validated predictions of subject 6's mental workload throughout the 2.5-h experimental session, which showed a Pearson's correlation coefficient of 0.89 with the actual *N* levels that the subject experienced. Together, these results show that the EEG and EOG data collected by the e-tattoo system contained sufficient information for a reliable estimation of the mental workload evoked by the dual *N*-back task in each of the six subjects.

DISCUSSION

This study introduces a wireless forehead wearable e-tattoo that integrates EEG and EOG sensors to assess mental workload. The e-tattoo platform consists of disposable large-area e-tattoos with adhesive electrodes and reusable small-footprint FPC, connected through ACF. The APC-GPU electrodes achieved remarkably low contact impedance and strong adhesion with the forehead skin, enabling long-term stable wear and high-fidelity EEG/EOG measurements, even during dynamic activities such as walking and running. This is a significant advantage compared to state-of-the-art wearables with exogenous form factors such as glasses and headbands or other devices that include bulky components and cables. Compared to commercial EEG systems that use gel electrodes, the wireless e-tattoo system demonstrated comparable signal fidelity and the ability to capture equivalent neural spectra from the forehead. We conducted dual *N*-back experiments on six subjects wearing the wireless e-tattoo in a controlled laboratory setting and obtained NASA-TLX-based self-assessment, task performance metrics, and physiological features. A random forest-based workload estimation model, trained on forehead EEG and EOG features evaluated from minimally processed raw signals from the e-tattoo, indicates the potential of the e-tattoo as a robust ambulatory cognitive-state-monitoring platform.

While many previous studies have explored individual aspects, such as electrode materials or manufacturing techniques, our key innovation lies in the successful decoding of mental workload using a wireless, low-power, low-noise, and ultra-thin EEG/EOG e-tattoo device. It addresses the unique challenges of monitoring forehead EEG and EOG, where wearability, non-obstructiveness, and signal stability are critical to assessing mental workload in the real world. By combining material innovation, cost-effective fabrication, custom circuit design, and reusable FPC configuration, our work offers an accessible and user-friendly solution that is distinct from both conventional rigid/semi-rigid EEG systems as well as reported peer e-tattoos for wearable neurotechnology.

Despite its promising capabilities, the current forehead e-tattoo system can be further improved. Long-term wearability of the e-tattoo depends on both stable skin contact and effective sweat management. Although our results show that sweating reduces the contact impedance by enhancing the ionic conductivity, excessive sweat could still compromise adhesion and reduce comfort. Studies have shown that molecules containing catechol groups, such as tannic acid[84] and polydopamine,[85] can form stable bonds with the skin even under sweating conditions through multiple interactions, including hydrogen bonding, π-π stacking, and covalent bonding. Furthermore, more liquid-permeable[86] or sweat-wicking[87] substrates can be employed to enhance long-term wearability.

In addition to limited breathability, APC-GPU electrodes are not compatible with hair, restricting the e-tattoo to the hairless area of the forehead. Although the prefrontal regions provide valuable information about cognitive engagement and attention, other brain regions, such as the frontocentral, temporal, and occipital regions, also contain information relevant to monitoring various neural activities related to emotional processing,

Please cite this article in press as: Huh et al., A wireless forehead e-tattoo for mental workload estimation, Device (2025), https://doi.org/10.1016/j.device.2025.100781

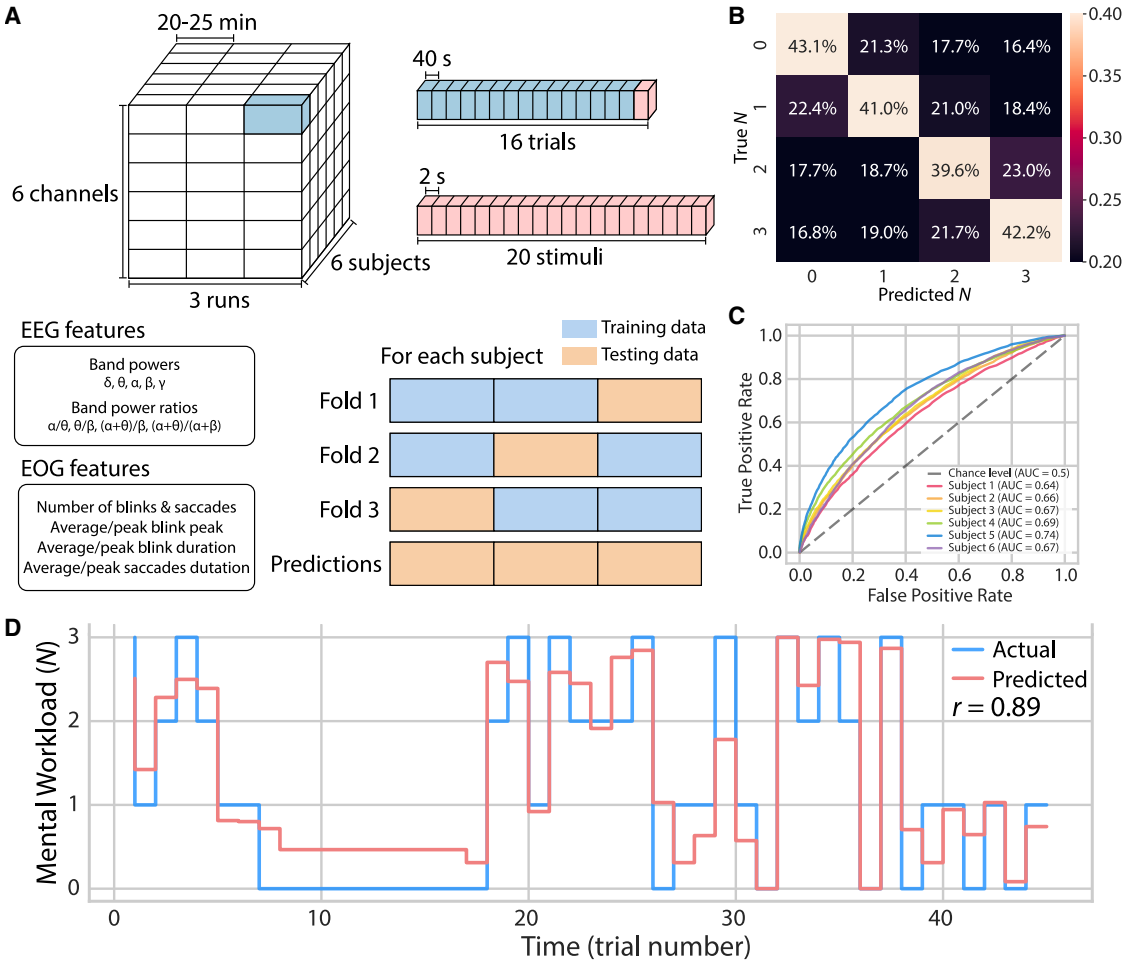

Figure 6. Mental workload estimation

(A) Overall *N*-back dataset structure and approach for mental workload estimation. The dataset is split into either trials for trial-level regression or further into individual stimuli for stimulus-level classification. Extracted EEG and EOG features are listed. All evaluations are based on a 3-fold cross-validation.

(B) Confusion matrix for all subjects from the four-class stimulus-level classification of *N*.

(C) Micro-averaged one-versus-rest (OvR) receiver operating characteristic (ROC) curves of each subject compared to that of a random unskilled classifier, defined as the chance level.

(D) Predicted mental workload over time (trials) by the random forest regression model for the best-performing subject (subject 6).

contextual attention, and working memory beyond the frontal regions. The absence of EEG recordings from these locations potentially limits the comprehensive assessment of mental workload in complex operational environments. Future research could benefit from integrating hair-compatible ultra-thin electrodes or e-tattoos[46,88,89] to extend the coverage area without impeding other headgear such as helmets or VR headsets.

In addition, in this study, we validated the ability of the device to assess mental workload in laboratory settings. Future work needs to be done to explore the feasibility of using the forehead e-tattoo platform for online estimation of mental workload during real-world human-machine interaction tasks that require optimal performance. One area needing improvement is to reduce the error of mental workload classification as well as address the potential mismatch between the experimental task used (dual *N*-back) and the realistic application. Although the presented system achieved an above-chance four-class classification in the *N*-back task, the performance of the predictive model could be potentially improved by additional feature engineering, increased training dataset size through a larger number of subjects or a data-generative model, and the use of less-explainable but higher-performing models (e.g., deep learning). While feature fusion between different modalities could improve accuracy, our study used EEG and EOG features separately. The presented system could also be expanded and validated to monitor other mental states and disorders, such as vigilance, stress, and sleep disorders. The multimodal approach, which integrates both EEG and EOG, could provide more detailed insight into the neurophysiological correlates of these conditions, opening avenues for early detection, warning, and personalized intervention. Although the proposed e-tattoo system is thin and helmet or VR headset compatible, further miniaturization and system

Please cite this article in press as: Huh et al., A wireless forehead e-tattoo for mental workload estimation, Device (2025), https://doi.org/10.1016/j.device.2025.100781

integration would improve its practicality in real-world long-term monitoring and data collection, overcoming the current limitations of traditional laboratory-based studies and equipment. This could in turn pave the way for larger-scale studies and longitudinal investigations, ultimately advancing human-machine interfaces based on EEG and EOG in everyday life.

METHODS

Materials and fabrication of the wireless forehead e-tattoo

The wireless forehead e-tattoo consists of two components: a soft sensor patch and a flexible DAQ module. The tattoo-like soft sensor patches were designed to fit each study subject's facial proportions. The soft sensor patch comprises a carrying top 3M Tegaderm layer (3M, USA), an electrode layer, and an insulating bottom Tegaderm layer (Figure S2). The stretchable filamentary-serpentine-shaped electrode layer made of GPU (Mineral Seal Corporation, China) was fabricated using our established cut-and-paste method. According to a previous report,[58] APC was made by adding supramolecular solvents (citric acid and β-cyclodextrin) and elastic polymer networks (chemically crosslinked PVA networks with glutaraldehyde) to the aqueous solution of PEDOT:PSS (Heraeus, USA). The detailed process of APC solution preparation is illustrated in Figure S18. A homogeneous mixture of APC was obtained by DAC 330-100SE (FlackTek Speed Mixer, USA). APC solution was blade coated on GPU at the active sensing locations and evaporated water in an oven at 70° C for 2 h. Then, the electrode layer was transferred to the carrying Tegaderm layer and encapsulated by the bottom Tegaderm layer while only exposing the APC-coated sensing locations and connecting pads to the DAQ circuits. The detailed fabrication process of the sensor patch is illustrated in Figure S19.

The FPC is divided into several islands connected by serpentine traces to improve stretchability and also for isolation between power, analog, and digital signals. The FPC is powered by a 150-mAh LiPo battery modified with an FPC connector (5034800400, Molex, USA), into which the FPC is directly inserted. For power management, we used low-noise, low-dropout regulators TPS7A2025 and LM27761 (both from Texas Instruments, USA) to create 2.5- and 5-V rails. The analog front end consists of the ADS1299 24-bit ADC (Texas Instruments, USA), which is connected via the SPI to the nRF52832 BLE system on a chip (Nordic Semiconductor, Norway). The nRF52832 was programmed with a low-power design firmware with the SWD interface. All the components were mounted on a 0.1-mm-thick double-layer FPC with electroless nickel immersion gold treatment for exposed copper. The thickness of the FPC was brought to 0.3 mm at select areas by a polyimide stiffener (for the battery input terminal) or an FR-4 stiffener (for under the large ICs). All chip components were hand soldered on the FPC (manufactured by PCBWay, China). The circuit components (Figure S20) include the ADS1299 24-bit ADC (Texas Instruments, USA) for signal amplification and conversion and nRF52832 BLE SoC (Nordic Semiconductor, Norway) for wireless transmission of data. The circuit features a low-noise design with the use of signal isolation, shielding, and low-noise components. All components were encapsulated in silicone compound (Silbione, Elkem, Norway) for better strain isolation and electrical shielding. An anisotropic conductive film (9703, 3M, USA) was used to bind and electrically connect the electrode layer to the channel pads on the FPC. A skin-safe medical adhesive was applied under the silicon casing to fix the circuits on the patch.

Characterization of APC-GPU electrodes

The SEM images of APC-GPU electrodes were obtained by Quanta 650 environmental scanning electron microscope (FEI Company, USA). The surface profile images and roughness were obtained using the VK-X1100 optical profilometer (Keyence, Japan) and the Multi File Analyzer application (Keyence, Japan). The stress-strain data and adhesion force of electrode films were measured by RSA-G2 solids analyzer (TA Instruments, USA). The sheet resistance of the films (n = 5 per film type) was measured by a DM3065 digital multimeter (RIGOL, China). Lastly, the skin-electrode contact impedance of the electrodes was measured with Autolab PGSTAT204 electrochemical workstation (Metrohm, Switzerland). Solid gel, GPU, and APC-GPU electrodes were applied to the forehead of study subjects (n = 4), and their contact impedance data were recorded every 10 min for the first hour after application and every 30 min afterward.

Characterization of DAQ module

Current-draw measurements were made with the Power Profiler Kit II (Nordic Semiconductor, Norway) on source mode. The RLD performance in different configurations was compared in both simulation and actual measurements with the e-tattoo. Simulations were conducted on QSPICE (Qorvo, USA) using the test circuit shown in Figure S5. To measure packet loss, we made recordings at various device-phone distances of below 1 or 10 m with no physical obstacles and calculated the packet loss by counting missing increments in the packet ID included in each data packet.

Study subjects and experiment setups

Six study subjects (four males and two females, age 20–33 years) were recruited. All subjects were required to perform two simple tests: eye open-closed and dual N-back. All experimental protocols were approved by the IRB of the University of Texas at Austin (STUDY00002937-MOD02). All study subjects were given a comprehensive set of instructions regarding the experiment protocol and provided written consent to agree on their voluntary participation in the study. Proper skin preparation was performed on the participants' mastoids and forehead area with Nuprep Skin Prep Gel (Weaver and Company, USA) and alcohol wipes before applying the wireless forehead e-tattoos and actiCAP active electrode with Brain Vision LiveAmp 32-ch amplifier (Brain Products, Germany). The biosignals were recorded simultaneously from both systems at AF7, Fp1, Fp2, and AF8 with a sampling rate of 250 Hz. In addition, hEOG and vEOG were collected from the e-tattoo. Sampled data from two systems and task event markers were transmitted to a computer via BLE and synchronized by the lab streaming layer (LSL) library.[65] The forehead e-tattoo attachment procedure begins with the EEG electrodes on the forehead, followed by the EOG

electrodes. Once these electrodes are secured, the reference and ground electrodes are placed on the mastoid bone behind the ears. Finally, the battery is attached and positioned in the designated pocket above the FPC module.

EEG/EOG pre-processing and feature extraction

All physiological data collected for this study were post-processed offline for evaluation and machine learning. First, EEG signals were bandpass filtered from 0.1 to 50 Hz. The following bands were defined to extract band power features: delta 1–4 Hz, theta 4–8 Hz, alpha 8–13 Hz, beta 13–30 Hz, and gamma 30–50 Hz. Ratios of band powers were also of particular interest in our study due to their popular use in related studies. Specifically, these ratios were evaluated: alpha/theta, which has been associated with mental workload[90]; theta/beta and (alpha + theta)/(alpha + beta), which have been associated with fatigue[91,92]; and beta/(alpha + theta), also known as the engagement index, which has been associated with task workload.[93] However, recent work has suggested that raw band powers and their ratios may not accurately represent oscillatory activity modulation information that is intended to be captured by the use of such measures.[94] In light of this, we incorporated a method of neural spectra parameterization proposed by Donoghue et al.,[95] which extracts periodic and aperiodic components from a given EEG power spectrum. The power spectrum with the aperiodic component removed, also referred to as a flattened spectrum, was used to calculate band power and band-power ratio measures in this study to ensure an accurate evaluation of oscillatory activity modulation.

EOG signals were bandpass filtered from 0.02 to 50 Hz. EOG features were extracted by an offline implementation of the algorithm proposed by Toivanen et al.,[96] which takes horizontal and vertical EOG inputs to estimate blink and saccade timings and durations based on an expectation maximization algorithm. From this output, the number of blinks, saccades, their durations and the ABP amplitude were collected as features. The model also outputs the probability of an extracted event indeed being an event of that type (possible types are blink, saccade, or fixation), the sum of which was also used as a feature to represent blink/saccade frequency weighted by the model's confidence.

Random forest model training and evaluation for mental workload prediction

Each channel-run-subject block containing approximately 20–25 min of e-tattoo data (with variable duration due to NASA-TLX administration) was divided into either 16 epochs of 40 s for trial-level regression or further divided into 16× 20 epochs of 1.8 s for stimulus-level classification (Figure 6A). The latter approach provides a more systematic evaluation of the predictive power of the extracted EEG features through a four-class classification of subject data collected during thousands of individual *N*-back stimulus presentations. The former approach provides a more reliable and continuous estimate of mental workload by using longer data segments, which allowed for a meaningful inclusion of EOG features, as opposed to the stimulus-level approach where the majority of the 1.8-s data segments were lacking blinks or saccades, resulting in a sparse feature matrix. Both approaches were evaluated with subject-specific 3-fold cross-validation, in which the model was always predicting the task difficulty *N* only based on unseen training data. To further reduce the risk of overfitting, the number of trees in the random forest classifier was increased to 500, which decreases the generalization error.

The stimulus-level classification was evaluated by an all-subject confusion matrix (Figure 6B) and subject-specific ROC curves (Figure 6C). To best capture the model's performance in predicting each class, we plotted the micro-averaged OvR ROC curves. This approach reflects the model's performance in predicting in each of the four *N* levels while accounting for class imbalance arising from rejected epochs due to significant motion. In this approach, each ROC curve in Figure 6C is a weighted average of four ROC curves for that subject (N = 0 vs. N = 1 or 2 or 3, N = 1 vs. N = 0 or 2 or 3, and so on). To clarify, the OvR paradigm is used only for the purpose of visualizing the two-dimensional ROC curves; the actual classification results presented in Figure 6B are the results of a true four-class classification without an OvR constraint.

RESOURCE AVAILABILITY

Lead contact

Requests for further information and resources should be directed to and will be fulfilled by the lead contact, Nanshu Lu (nanshulu@utexas.edu).

Materials availability

The method section lists all materials used in this study, which are commercially available. This study did not generate new materials.

Data and code availability

The authors declare that the data supporting the findings of this study are available within the article and its supplemental information files as well as from the corresponding author upon reasonable request. Physiological data of study participants are not disclosed due to IRB review (STUDY00002937-MOD02).

ACKNOWLEDGMENTS

N.L. acknowledges the support from the US Army Research Office under Cooperative Agreement W911NF-19-2-0333. The views and conclusions contained in this article are those of the authors and should not be interpreted as representing the official policies, either expressed or implied, of the US Army Research Office or the US government.

AUTHOR CONTRIBUTIONS

Conceptualization, N.L.; methodology, H.H., H.S., and N.L.; software, H.H., H.S., and K.H.; validation, H.H., H.S., and H.L.; formal analysis, H.H. and H.S.; investigation, H.H., C.H., S.T., and H.S., data curation, H.H. and H.S.; writing – original draft, H.H., H.S., and N.L.; writing – review & editing, H.H., H.S., M.D., K.A.F., L.S., and N.L.; visualization, H.H., H.S., and N.L.; supervision, L.S. and N.L.; project administration, H.H., H.S., and N.L.; funding acquisition, K.A.F., L.S., and N.L.

DECLARATION OF INTERESTS

The authors declare no competing interests.

SUPPLEMENTAL INFORMATION

Supplemental information can be found online at https://doi.org/10.1016/j.device.2025.100781.

Received: January 13, 2025
Revised: March 21, 2025
Accepted: April 8, 2025
Published: May 29, 2025

REFERENCES

1. Wickens, C.D. (2002). Multiple resources and performance prediction. Theor. Issues Ergon. Sci. *3*, 159–177. https://doi.org/10.1080/14639220210123806.
2. Berka, C., Levendowski, D.J., Lumicao, M.N., Yau, A., Davis, G., Zivkovic, V.T., Olmstead, R.E., Tremoulet, P.D., and Craven, P.L. (2007). Eeg correlates of task engagement and mental workload in vigilance, learning, and memory tasks. Aviat Space Environ. Med. *78*, B231–B244.
3. Galy, E., Cariou, M., and Mélan, C. (2012). What is the relationship between mental workload factors and cognitive load types? Int. J. Psychophysiol. *83*, 269–275.
4. Babiloni, F. (2019). Mental workload monitoring: New perspectives from neuroscience. Communications in Computer and Information Science *1107*, 3–19. https://doi.org/10.1007/978-3-030-32423-0_1.
5. Lyu, T., Song, W., and Du, K. (2019). Human factors analysis of air traffic safety based on hfacs-bn model. Appl. Sci. *9*, 5049. https://doi.org/10.3390/app9235049.
6. Pape, A.M., Wiegmann, D.A., and Shappell, S. (2001). Air traffic control (atc) related accidents and incidents: a human factors analysis. In Focusing Attention on Aviation Safety: the 11th International Symposium on Aviation Psychology.
7. Kantowitz, B.H., and Simsek, O. (2001). Secondary-task measures of driver workload. In Secondary-task measures of driver workload (CRC Press).
8. Paxion, J., Galy, E., and Berthelon, C. (2014). Mental workload and driving. Front. Psychol. *5*, 1344. https://doi.org/10.3389/fpsyg.2014.01344.
9. Borghini, G., Astolfi, L., Vecchiato, G., Mattia, D., and Babiloni, F. (2014). Measuring neurophysiological signals in aircraft pilots and car drivers for the assessment of mental workload, fatigue and drowsiness. Neurosci. Biobehav. Rev. *44*, 58–75.
10. Martins, A.P.G. (2016). A review of important cognitive concepts in aviation. Aviation *20*, 65–84. https://doi.org/10.3846/16487788.2016.1196559.
11. Feltman, K.A., Vogl, J.F., McAtee, A., and Kelley, A.M. (2024). Measuring aviator workload using eeg: an individualized approach to workload manipulation. Front. Neuroergon. *5*, 1397586.
12. Edwards, T., Martin, L., Bienert, N., and Mercer, J. (2017). The relationship between workload and performance in air traffic control: Exploring the influence of levels of automation and variation in task demand. Communications in Computer and Information Science *726*, 120–139. https://doi.org/10.1007/978-3-319-61061-0_8.
13. Aricò, P., Borghini, G., Di Flumeri, G., Colosimo, A., Bonelli, S., Golfetti, A., Pozzi, S., Imbert, J.P., Granger, G., Benhacene, R., and Babiloni, F. (2016). Adaptive automation triggered by eeg-based mental workload index: a passive brain-computer interface application in realistic air traffic control environment. Front. Hum. Neurosci. *10*, 539.
14. Landi, C.T., Villani, V., Ferraguti, F., Sabattini, L., Secchi, C., and Fantuzzi, C. (2018). Relieving operators' workload: Towards affective robotics in industrial scenarios. Mechatronics *54*, 144–154, URL:. https://doi.org/10.1016/j.mechatronics.2018.07.012 https://www.sciencedirect.com/science/article/pii/S0957415818301260
15. Longo, L., Wickens, C.D., Hancock, G., and Hancock, P.A. (2022). Human mental workload: A survey and a novel inclusive definition. Front. Psychol. *13*, 883321. https://doi.org/10.3389/fpsyg.2022.883321.
16. Hart, S.G., and Staveland, L.E. (1988). Development of nasa-tlx (task load index): Results of empirical and theoretical research. Adv. Psychol. *52*, 139–183. https://doi.org/10.1016/s0166-4115(08)62386-9.
17. Longo, L. (2015). A defeasible reasoning framework for human mental workload representation and assessment. Behav. Inf. Technol. *34*, 758–786. https://doi.org/10.1080/0144929x.2015.1015166.
18. Stanton, N.A., Salmon, P.M., Rafferty, L.A., Walker, G.H., Baber, C., and Jenkins, D.P. (2017). Human Factors Methods: A Practical Guide for Engineering and Design (Taylor and Francis).
19. Lenneman, J.K., and Backs, R.W. (2009). Cardiac autonomic control during simulated driving with a concurrent verbal working memory task. Hum. Factors *51*, 404–418.
20. Hogervorst, M.A., Brouwer, A.M., and van Erp, J.B.F. (2014). Combining and comparing eeg, peripheral physiology and eye-related measures for the assessment of mental workload. Front. Neurosci. *8*, 322.
21. Wilson, G.F. (2002). An analysis of mental workload in pilots during flight using multiple psychophysiological measures. Int. J. Aviat. Psychol. *12*, 3–18. https://doi.org/10.1207/s15327108ijap1201_2.
22. Bachurina, V., and Arsalidou, M. (2022). Multiple levels of mental attentional demand modulate peak saccade velocity and blink rate. Heliyon *8*, e08826. https://doi.org/10.1016/j.heliyon.2022.e08826.
23. Beatty, J. (1982). Task-evoked pupillary responses, processing load, and the structure of processing resources. Psychol. Bull. *91*, 276–292. https://doi.org/10.1037/0033-2909.91.2.276.
24. Gonzalez-Sanchez, J., Baydogan, M., Chavez-Echeagaray, M.E., Atkinson, R.K., and Burleson, W. (2017). Chapter 11 - affect measurement: A roadmap through approaches, technologies, and data analysis. In Emotions and Affect in Human Factors and Human-Computer Interaction, M. Jeon, ed. (San Diego: Academic Press), pp. 255–288. https://doi.org/10.1016/B978-0-12-801851-4.00011-2.
25. Tangsgaard Hvelplund, K. (2014). Eye tracking and the translation process: Reflections on the analysis and interpretation of eye-tracking data. MonTI. *special issue 1*, 201–223. https://doi.org/10.6035/monti.2014.ne1.6.
26. Pettersson, K., Jagadeesan, S., Lukander, K., Henelius, A., Haeggström, E., and Müller, K. (2013). Algorithm for automatic analysis of electro-oculographic data. Biomed. Eng. Online *12*, 110. https://doi.org/10.1186/1475-925x-12-110.
27. Jia, Y., and Tyler, C.W. (2019). Measurement of saccadic eye movements by electrooculography for simultaneous eeg recording. Behav. Res. Methods *51*, 2139–2151. https://doi.org/10.3758/s13428-019-01280-8.
28. Abe, T. (2023). Perclos-based technologies for detecting drowsiness: Current evidence and future directions. Sleep Adv. *4*, zpad006. https://doi.org/10.1093/sleepadvances/zpad006.
29. Cori, J.M., Anderson, C., Shekari Soleimanloo, S., Jackson, M.L., and Howard, M.E. (2019). Narrative review: Do spontaneous eye blink parameters provide a useful assessment of state drowsiness? Sleep Med. Rev. *45*, 95–104. https://doi.org/10.1016/j.smrv.2019.03.004.
30. Abe, T., Mishima, K., Kitamura, S., Hida, A., Inoue, Y., Mizuno, K., Kaida, K., Nakazaki, K., Motomura, Y., Maruo, K., et al. (2020). Tracking intermediate performance of vigilant attention using multiple eye metrics. Sleep *43*, zsz219. https://doi.org/10.1093/sleep/zsz219.
31. Mahmood, M., Kwon, S., Kim, H., Kim, Y.S., Siriaraya, P., Choi, J., Otkhmezuri, B., Kang, K., Yu, K.J., Jang, Y.C., et al. (2021). Wireless soft scalp electronics and virtual reality system for motor imagery-based brain–machine interfaces. Adv. Sci. *8*, 2101129.
32. López-Larraz, E., Escolano, C., Robledo-Menéndez, A., Morlas, L., Alda, A., and Minguez, J. (2023). A garment that measures brain activity: Proof of concept of an eeg sensor layer fully implemented with smart textiles. Front. Hum. Neurosci. *17*, 1135153. https://doi.org/10.3389/fnhum.2023.1135153.
33. Lin, C.T., Chuang, C.H., Cao, Z., Singh, A.K., Hung, C.S., Yu, Y.H., Nascimben, M., Liu, Y.T., King, J.T., Su, T.P., and Wang, S.J. (2017). Forehead eeg in support of future feasible personal healthcare solutions: Sleep management, headache prevention, and depression treatment. IEEE Access *5*, 10612–10621. https://doi.org/10.1109/access.2017.2675884.

34. Debellemaniere, E., Chambon, S., Pinaud, C., Thorey, V., Dehaene, D., Léger, D., Chennaoui, M., Arnal, P.J., and Galtier, M.N. (2018). Performance of an ambulatory dry-eeg device for auditory closed-loop stimulation of sleep slow oscillations in the home environment. Front. Hum. Neurosci. *12*, 88. https://doi.org/10.3389/fnhum.2018.00088.

35. Kim, S.W., Lee, K., Yeom, J., Lee, T.H., Kim, D.H., and Kim, J.J. (2020). Wearable multi-biosignal analysis integrated interface with direct sleep-stage classification. IEEE Access *8*, 46131–46140. https://doi.org/10.1109/ACCESS.2020.2978391.

36. Banville, H., Wood, S.U.N., Aimone, C., Engemann, D.A., and Gramfort, A. (2022). Robust learning from corrupted eeg with dynamic spatial filtering. Neuroimage *251*, 118994. https://doi.org/10.1016/j.neuroimage.2022.118994.

37. Kosmyna, N., Morris, C., Sarawgi, U., Nguyen, T., and Maes, P. (2019). Attentivu: A wearable pair of eeg and eog glasses for real-time physiological processing. In 2019 IEEE 16th International Conference on Wearable and Implantable Body Sensor Networks (BSN), pp. 1–4. https://doi.org/10.1109/BSN.2019.8771080.

38. Xu, Y., De la Paz, E., Paul, A., Mahato, K., Sempionatto, J.R., Tostado, N., Lee, M., Hota, G., Lin, M., Uppal, A., et al. (2023). In-ear integrated sensor array for the continuous monitoring of brain activity and of lactate in sweat. Nat. Biomed. Eng. *7*, 1307–1320.

39. Belkhiria, C., and Peysakhovich, V. (2021). Eog metrics for cognitive workload detection. Procedia Comput. Sci. *192*, 1875–1884. https://doi.org/10.1016/j.procs.2021.08.193.

40. Shustak, S., Inzelberg, L., Steinberg, S., Rand, D., David Pur, M., Hillel, I., Katzav, S., Fahoum, F., De Vos, M., Mirelman, A., and Hanein, Y. (2019). Home monitoring of sleep with a temporary-tattoo eeg, eog and emg electrode array: A feasibility study. J. Neural. Eng. *16*, 026024. https://doi.org/10.1088/1741-2552/aafa05.

41. Mishra, S., Kim, Y.S., Intarasirisawat, J., Kwon, Y.T., Lee, Y., Mahmood, M., Lim, H.R., Herbert, R., Yu, K.J., Ang, C.S., and Yeo, W.H. (2020). Soft, wireless periocular wearable electronics for real-time detection of eye vergence in a virtual reality toward mobile eye therapies. Sci. Adv. *6*, eaay1729. https://doi.org/10.1126/sciadv.aay1729.

42. Shin, J.H., Kwon, J., Kim, J.U., Ryu, H., Ok, J., Joon Kwon, S., Park, H., and Kim, T.i. (2022). Wearable eeg electronics for a brain–ai closed-loop system to enhance autonomous machine decision-making. npj Flex. Electron. *6*, 32. https://doi.org/10.1038/s41528-022-00164-w.

43. Araki, T., Yoshimoto, S., Uemura, T., Miyazaki, A., Kurihira, N., Kasai, Y., Harada, Y., Nezu, T., Iida, H., Sandbrook, J., et al. (2022). Skin-like transparent sensor sheet for remote healthcare using electroencephalography and photoplethysmography. Adv. Mater. Technol. *7*, 2200362.

44. Reis Carneiro, M., Majidi, C., and Tavakoli, M. (2022). Multi-electrode printed bioelectronic patches for long-term electrophysiological monitoring. Adv. Funct. Mater. *32*, 2205956.

45. Kwon, S., Kim, H.S., Kwon, K., Kim, H., Kim, Y.S., Lee, S.H., Kwon, Y.T., Jeong, J.W., Trotti, L.M., Duarte, A., and Yeo, W.H. (2023). At-home wireless sleep monitoring patches for the clinical assessment of sleep quality and sleep apnea. Sci. Adv. *9*, eadg9671.

46. de Vasconcelos, L.S., Yan, Y., Maharjan, P., Kumar, S., Zhang, M., Yao, B., Li, H., Duan, S., Li, E., Williams, E., et al. (2025). On-scalp printing of personalized electroencephalography e-tattoos. Cell Biomaterials *1*, 100004.

47. Tian, L., Zimmerman, B., Akhtar, A., Yu, K.J., Moore, M., Wu, J., Larsen, R. J., Lee, J.W., Li, J., Liu, Y., et al. (2019). Large-area mri-compatible epidermal electronic interfaces for prosthetic control and cognitive monitoring. Nat. Biomed. Eng. *3*, 194–205.

48. Ferrari, L.M., Ismailov, U., Badier, J.M., Greco, F., and Ismailova, E. (2020). Conducting polymer tattoo electrodes in clinical electro- and magneto-encephalography. npj Flex. Electron. *4*, 4–9.

49. Yoshimoto, S., Araki, T., Uemura, T., Nezu, T., Kondo, M., Sasai, K., Iwase, M., Satake, H., Yoshida, A., Kikuchi, M., and Sekitani, T. (2016). Wireless eeg patch sensor on forehead using on-demand stretchable electrode sheet and electrode-tissue impedance scanner. In 2016 38th Annual International Conference of the IEEE Engineering in Medicine and Biology Society (EMBC) (IEEE), pp. 6286–6289. https://doi.org/10.1109/EMBC.2016.7592165.

50. EHRENBERG, J.A., and EPSTEIN, C.M. (2017). Technical aspects of ambulatory electroencephalography. In Ambulatory EEG Monitoring, W. O. Tatum, ed. (New York: Springer Publishing Company), pp. 13–32. https://doi.org/10.1891/9781617052781.0002.

51. Sauseng, P., Griesmayr, B., Freunberger, R., and Klimesch, W. (2010). Control mechanisms in working memory: a possible function of eeg theta oscillations. Neurosci. Biobehav. Rev. *34*, 1015–1022.

52. Herff, C., Heger, D., Fortmann, O., Hennrich, J., Putze, F., and Schultz, T. (2013). Mental workload during n-back task—quantified in the prefrontal cortex using fnirs. Front. Hum. Neurosci. *7*, 935.

53. Yang, S., Chen, Y.C., Nicolini, L., Pasupathy, P., Sacks, J., Su, B., Yang, R., Sanchez, D., Chang, Y.F., Wang, P., et al. (2015). Cut-and-paste" manufacture of multiparametric epidermal sensor systems. Adv. Mater. *27*, 6423–6430.

54. Lu, N., and Yang, S. (2015). Mechanics for stretchable sensors. Curr. Opin. Solid State Mater. Sci. *19*, 149–159, Mechanics of Stretchable Electronics. https://doi.org/10.1016/j.cossms.2014.12.007.

55. Bhattacharya, S., Nikbakht, M., Alden, A., Tan, P., Wang, J., Alhalimi, T.A., Kim, S., Wang, P., Tanaka, H., Tandon, A., et al. (2023). A chest-conformable, wireless electro-mechanical e-tattoo for measuring multiple cardiac time intervals. Adv. Electron. Mater. *9*, 2201284. https://doi.org/10.1002/aelm.202201284.

56. Jeong, H., Wang, L., Ha, T., Mitbander, R., Yang, X., Dai, Z., Qiao, S., Shen, L., Sun, N., and Lu, N. (2019). Modular and reconfigurable wireless e-tattoos for personalized sensing. Adv. Mater. Technol. *4*, 1900117. https://doi.org/10.1002/admt.201900117.

57. Wang, L., and Lu, N. (2016). Conformability of a thin elastic membrane laminated on a soft substrate with slightly wavy surface. J. Appl. Mech. *83*, 041007, URL:. https://doi.org/10.1115/1.4032466

58. Tan, P., Wang, H., Xiao, F., Lu, X., Shang, W., Deng, X., Song, H., Xu, Z., Cao, J., Gan, T., et al. (2022). Solution-processable, soft, self-adhesive, and conductive polymer composites for soft electronics. Nat. Commun. *13*, 358.

59. Ludwig, K.A., Uram, J.D., Yang, J., Martin, D.C., and Kipke, D.R. (2006). Chronic neural recordings using silicon microelectrode arrays electrochemically deposited with a poly (3, 4-ethylenedioxythiophene)(pedot) film. J. Neural. Eng. *3*, 59–70.

60. Shin, J.H., Choi, J.Y., June, K., Choi, H., and Kim, T.i. (2024). Polymeric conductive adhesive-based ultrathin epidermal electrodes for long-term monitoring of electrophysiological signals. Adv. Mater. *36*, 2313157.

61. Kihara, A. (2016). Synthesis and degradation pathways, functions, and pathology of ceramides and epidermal acylceramides. Prog. Lipid Res. *63*, 50–69.

62. Wu, S., Cai, C., Li, F., Tan, Z., and Dong, S. (2020). Deep eutectic supramolecular polymers: Bulk supramolecular materials. Angew Chem. Int. Ed. Engl. *59*, 11871–11875.

63. Qu, J., Ouyang, L., Kuo, C.c., and Martin, D.C. (2016). Stiffness, strength and adhesion characterization of electrochemically deposited conjugated polymer films. Acta Biomater. *31*, 114–121.

64. Falland-Cheung, L., Scholze, M., Lozano, P.F., Ondruschka, B., Tong, D. C., Brunton, P.A., Waddell, J.N., and Hammer, N. (2018). Mechanical properties of the human scalp in tension. J. Mech. Behav. Biomed. Mater. *84*, 188–197.

65. Swartz Center for Computational Neuroscience . Lab streaming layer. . https://github.com/sccn/labstreaminglayer.

66. Barry, R.J., Clarke, A.R., Johnstone, S.J., Magee, C.A., and Rushby, J.A. (2007). Eeg differences between eyes-closed and eyes-open resting conditions. Clin. Neurophysiol. *118*, 2765–2773.

67. Kanoh, S., Ichi-nohe, S., Shioya, S., Inoue, K., and Kawashima, R. (2015). Development of an eyewear to measure eye and body movements. In 2015 37th Annual International Conference of the IEEE Engineering in Medicine and Biology Society (EMBC) (IEEE). https://doi.org/10.1109/embc.2015.7318844.

68. Heo, J., Yoon, H., and Park, K.S. (2017). A novel wearable forehead eog measurement system for human computer interfaces. Sensors *17*, 1485. https://doi.org/10.3390/s17071485.

69. Gwin, J.T., Gramann, K., Makeig, S., and Ferris, D.P. (2010). Removal of movement artifact from high-density eeg recorded during walking and running. J. Neurophysiol. *103*, 3526–3534.

70. Downey, R.J., and Ferris, D.P. (2023). icanclean removes motion, muscle, eye, and line-noise artifacts from phantom eeg. Sensors *23*, 8214.

71. He, D., Donmez, B., Liu, C.C., and Plataniotis, K.N. (2019). High cognitive load assessment in drivers through wireless electroencephalography and the validation of a modified n-back task. IEEE Trans. Hum. Mach. Syst. *49*, 362–371.

72. Pergher, V., Wittevrongel, B., Tournoy, J., Schoenmakers, B., and Van Hulle, M.M. (2019). Mental workload of young and older adults gauged with erps and spectral power during n-back task performance. Biol. Psychol. *146*, 107726. https://doi.org/10.1016/j.biopsycho.2019.107726.

73. Meule, A. (2017). Reporting and interpreting working memory performance in n-back tasks. Front. Psychol. *8*, 352. https://doi.org/10.3389/fpsyg.2017.00352.

74. Mikulka, P.J., Scerbo, M.W., and Freeman, F.G. (2002). Effects of a biocybernetic system on vigilance performance. Hum. Factors *44*, 654–664.

75. Esposito, F., Aragri, A., Piccoli, T., Tedeschi, G., Goebel, R., and Di Salle, F. (2009). Distributed analysis of simultaneous eeg-fmri time-series: modeling and interpretation issues. Magn. Reson. Imaging *27*, 1120–1130.

76. Jensen, O., and Tesche, C.D. (2002). Frontal theta activity in humans increases with memory load in a working memory task. Eur. J. Neurosci. *15*, 1395–1399.

77. Fink, A., Grabner, R.H., Neuper, C., and Neubauer, A.C. (2005). Eeg alpha band dissociation with increasing task demands. Brain Res. Cogn. Brain Res. *24*, 252–259.

78. Keil, A., Mussweiler, T., and Epstude, K. (2006). Alpha-band activity reflects reduction of mental effort in a comparison task: a source space analysis. Brain Res. *1121*, 117–127.

79. Lei, S., and Roetting, M. (2011). Influence of task combination on eeg spectrum modulation for driver workload estimation. Hum. Factors *53*, 168–179.

80. Waldhauser, G.T., Johansson, M., and Hanslmayr, S. (2012). Alpha/beta oscillations indicate inhibition of interfering visual memories. J. Neurosci. *32*, 1953–1961.

81. Zanto, T.P., and Gazzaley, A. (2009). Neural suppression of irrelevant information underlies optimal working memory performance. J. Neurosci. *29*, 3059–3066.

82. MacLean, M.H., Arnell, K.M., and Cote, K.A. (2012). Resting eeg in alpha and beta bands predicts individual differences in attentional blink magnitude. Brain Cognit. *78*, 218–229.

83. Mark, J.A., Curtin, A., Kraft, A.E., Ziegler, M.D., and Ayaz, H. (2024). Mental workload assessment by monitoring brain, heart, and eye with six biomedical modalities during six cognitive tasks. Front. Neuroergon. *5*, 1345507. https://doi.org/10.3389/fnrgo.2024.1345507.

84. Cao, J., Yang, X., Rao, J., Mitriashkin, A., Fan, X., Chen, R., Cheng, H., Wang, X., Goh, J., Leo, H.L., and Ouyang, J. (2022). Stretchable and self-adhesive pedot:pss blend with high sweat tolerance as conformal biopotential dry electrodes. ACS Appl. Mater. Interfaces *14*, 39159–39171. https://doi.org/10.1021/acsami.2c11921.

85. Han, Q., Zhang, C., Guo, T., Tian, Y., Song, W., Lei, J., Li, Q., Wang, A., Zhang, M., Bai, S., and Yan, X. (2023). Hydrogel nanoarchitectonics of a flexible and self-adhesive electrode for long-term wireless electroencephalogram recording and high-accuracy sustained attention evaluation. Adv. Mater. *35*, 2209606. https://doi.org/10.1002/adma.202209606.

86. Yang, Y., Cui, T., Li, D., Ji, S., Chen, Z., Shao, W., Liu, H., and Ren, T.L. (2022). Breathable electronic skins for daily physiological signal monitoring. Nano-Micro Lett. *14*, 161.

87. Zhang, B., Li, J., Zhou, J., Chow, L., Zhao, G., Huang, Y., Ma, Z., Zhang, Q., Yang, Y., Yiu, C.K., et al. (2024). A three-dimensional liquid diode for soft, integrated permeable electronics. Nature *628*, 84–92. https://doi.org/10.1038/s41586-024-07161-1.

88. Zhang, L., Kumar, K.S., He, H., Cai, C.J., He, X., Gao, H., Yue, S., Li, C., Seet, R.C.S., Ren, H., and Ouyang, J. (2020). Fully organic compliant dry electrodes self-adhesive to skin for long-term motion-robust epidermal biopotential monitoring. Nat. Commun. *11*, 4683.

89. Hsieh, J.C., He, W., Venkatraghavan, D., Koptelova, V.B., Ahmad, Z.J., Pyatnitskiy, I., Wang, W., Jeong, J., Tang, K.K.W., Harmeier, C., et al. (2024). Design of an injectable, self-adhesive, and highly stable hydrogel electrode for sleep recording. Device *2*, 100182.

90. Raufi, B., and Longo, L. (2022). An evaluation of the eeg alpha-to-theta and theta-to-alpha band ratios as indexes of mental workload. Front. Neuroinf. *16*, 861967. https://doi.org/10.3389/fninf.2022.861967.

91. van Son, D., De Blasio, F.M., Fogarty, J.S., Angelidis, A., Barry, R.J., and Putman, P. (2019). Frontal eeg theta/beta ratio during mind wandering episodes. Biol. Psychol. *140*, 19–27. https://doi.org/10.1016/j.biopsycho.2018.11.003.

92. Ismail, L.E., and Karwowski, W. (2020). Applications of eeg indices for the quantification of human cognitive performance: A systematic review and bibliometric analysis. PLoS One *15*, e0242857. https://doi.org/10.1371/journal.pone.0242857.

93. Prinzel, L.J., Freeman, F.G., Scerbo, M.W., Mikulka, P.J., and Pope, A.T. (2000). A closed-loop system for examining psychophysiological measures for adaptive task allocation. Int. J. Aviat. Psychol. *10*, 393–410. https://doi.org/10.1207/s15327108ijap1004_6.

94. Donoghue, T., Dominguez, J., and Voytek, B. (2020). Electrophysiological frequency band ratio measures conflate periodic and aperiodic neural activity. eneuro *7*, xxx. https://doi.org/10.1523/eneuro.0192-20.2020.

95. Donoghue, T., Haller, M., Peterson, E.J., Varma, P., Sebastian, P., Gao, R., Noto, T., Lara, A.H., Wallis, J.D., Knight, R.T., et al. (2020). Parameterizing neural power spectra into periodic and aperiodic components. Nat. Neurosci. *23*, 1655–1665. https://doi.org/10.1038/s41593-020-00744-x.

96. Toivanen, M., Pettersson, K., and Lukander, K. (2015). A probabilistic real-time algorithm for detecting blinks, saccades, and fixations from eog data. Journal of Eye Movement Research *8*, 2. https://bop.unibe.ch/JEMR/article/view/2398.